Department of Physics and Astronomy

University of Heidelberg

Diploma thesis

in Physics

submitted by

Stephan Burkhardt

born in Würzburg

2012

# Noise-assisted Interband Transitions in the Wannier-Stark Problem

This diploma thesis has been carried out by Stephan Burkhardt

at the

Institut für theoretische Physik der Universität Heidelberg

under the supervision of

Herrn Priv.-Doz. Sandro Wimberger

**Durch Rauschen unterstützte Interband-Übergänge im Wannier-Stark Problem**:

In dieser Arbeit untersuchen wir das Interband-Tunneln in gekippten bichromatischen optischen Gittern. Der Fokus der Arbeit liegt auf Systemen, in denen eines der Gitter von einem farbigen Rausch-Prozess ausgelenkt wird. Allerdings konnten wir auch interessante Effekte für ein System beobachten, in dem die beiden Gitter sich mit einer konstanten Relativgeschwindigkeit bewegen. In beiden Fällen analysieren wir die Systeme mit Hilfe eines vereinfachtes analytisches Modells, das wir anschließend mit den Ergebnissen von numerischen Simulationen vergleichen.
Für das gekippte bichromatische Gitter mit konstanter Relativgeschwindigkeit $\beta$ beobachten wir, dass das Interband-Tunneln für gewisse Werte $\beta$ extrem verstärkt wird. Wir führen ein Modell ein, das es erlaubt, diese Resultate zu interpretieren und sie qualitativ zu erklären.
Ähnliches Verhalten beobachten wir für das von Rauschen angetriebene Gitter. Hier beobachten wir, dass die Tunnelrate von Rausch-Prozessen einer speziellen Intensität maximiert wird. Obwohl das Modell, das wir für dieses System einführen, nur für sehr langsame Rauschprozesse exakt ist, kann es qualitativ selbst die numerischen Resultate für schnelles Rauschen erklären. Dieses Modell erlaubt es uns außerdem, Ergebnisse, die von Tayebirad et al. in vorherigen Arbeiten gefunden wurden [38], zu erklären.

**Noise-assisted Interband Transitions in the Wannier-Stark Problem**:

In this work we study the interband transport properties of a tilted bichromatic optical lattice. While our main interest is the behavior of this system when one of the lattices is driven by colored noise, we also present interesting results for the case where the two lattices are moving with a constant relative velocity. Simplified analytical models are employed, that draw a connection between those two systems. The predictions made by these models are then compared to results of extensive numerical simulations.
For the tilted bichromatic lattice with a constant relative velocity $\beta$ between the two lattices, we find that the interband tunneling is strongly enhanced for certain values of $\beta$. We furthermore propose a model that allows to interpret and qualitatively explain these results.
A similar behavior is witnessed for tilted noise-driven bichromatic lattices. We find that a noise process of a certain strength maximizes the tunneling rate. While the model we propose for this noise-driven case is only accurate for systems driven by slow noise, we find that it qualitatively explains the numerical results even for fast noise. Using this model we are moreover able to explain effects previously found by Tayebirad et al. [38].

# Acknowledgments

I would like to thank all those who made this thesis possible. Foremost, my gratitude goes to my supervisor Sandro Wimberger who through his support, helpful suggestions and insightful discussions enabled me to successfully work on and finish this thesis. I would moreover like to thank him for providing me the opportunity to visit the department of physics in Pisa in the beginning of this year.

There I met with Riccardo Mannella to whom I want to express my profound gratitude for not only forgiving me for repeatedly misspelling his name but moreover providing me with great advice and discussions about the problems I faced in my thesis at this point.

I also want to thank Ghazal Tayebirad, Carlos Parra-Murillo, Georgios Kordas, Julia Link and Anton Ivanov for providing a hospitable atmosphere, helping me out with problems and providing uplifting conversations. But most of all I would like to thank Matthias Kraft, who not only proofread large parts of my thesis but also helped me tremendously in better understanding the problem at hand.

Apart from my colleagues, my profound gratitude also goes to my girlfriend Rebecca, who supported me throughout the year and especially during the last months of my work on this thesis. I also want to thank my family for their emotional and financial support. Further thanks go to my two emergency-proofreaders Arne Klein and Paul Müller.

# Contents

# 1 Introduction

## 1.1 Background

The first realization of a Bose-Einstein condensate in 1995 paved the way for a wide range of experiments that allow the direct observation of quantum mechanical effects in highly controllable environments. Since then the control over the condensate and the forces it is subject to has been improved to such an extend that a wide range of quantum mechanical systems can today be realized and observed.

This fine control over the system allows to easily analyze many quantum mechanical effects that were previously not directly measurable or only realizable in systems that are hard to control and observe. These condensates can therefore be used as a sort of quantum simulator.

One such example are Bloch oscillations, a quantum mechanical effect first predicted for electrons in solid states. Due to the complicated nature of these solid state systems the effect was, however, not observable in these systems for a long time. While first observations were already possible in semiconductor superlattices in 1992 [23], using Bose-Einstein condensates in optical lattices allows today to induce, control and observe such oscillations for up to several seconds, corresponding to thousands of oscillation periods [18, 10].

In these and other experiments, optical lattices have proven an invaluable tool to observe effects previously predicted for solid state systems. Created by a standing laser light wave, these lattices form are a potential of sinusoidal shape which therefore resembles the potential experienced by electrons in a solid.

This means that the transport properties of Bose-Einstein condensates in optical lattices have many relations to properties of solid state materials. For this reason the transport of the condensate in a tilted optical lattice is a very worthwhile problem. This so-called Wannier-Stark system shows a combination of tunneling behavior, the previously mentioned Bloch oscillations and interesting phenomena that occur due to the interplay between those two effects [35, 47].

Since most naturally occurring systems are characterized by a certain degree of disorder, studying the effects of disordered potentials is necessary for a better understanding of many real-world systems. One example of an interesting effect that is caused by spatial disorder is Anderson localization, which inhibits diffusion in disordered potentials [43].

All real world systems that are not at zero temperature are disturbed by randomly fluctuating interactions with the outside world. For electrons in solid state materials this is, amongst others, the coupling to the phonon bath. It is thus also

interesting to study the transport properties of a system disturbed not by spatial but by temporal disorder.

In this work we will study the transport properties of a Wannier-Stark system which is disturbed by the presence of a second randomly fluctuating optical lattice. The analysis of this system will be performed by numerical simulations but also through the construction of a model that approximates the behavior of the full system. This model will enable us to better understand the influence the fluctuating lattice has on the Wannier-Stark system.

## 1.2 Overview

In this thesis we study a Wannier-Stark system under the influence of an additional, noise-driven lattice. We investigate the effect of this second lattice on the tunneling of the wavefunction out of the ground band. We devise a simplified model of the system which allows a better understanding of the influence of the noise lattice. The predictions of this model are then compared to the results of numerical simulations.
The following is a more detailed outline of this work:

**Chapter 2:** In this chapter we will introduce the system under consideration and provide the means which we need in the later chapters for analyzing this system.
In section 2.1 we describe Bose-Einstein tools and optical lattices, which are the tools required for an experimental implementation of the Wannier-Stark system. The Wannier-Stark system is then introduced in section 2.2. In this section we also explain how the emerging band structure influences transport in such a system and show how the system can be understood using the Landau-Zener approximation.
The stochastic differential equations needed for the definition of the noise process are introduced in section 2.3. We start with a short explanation of the general theory of stochastic differential equations and their properties. Thereafter the noise processes used in this work are defined. While their properties will be explained in this section, the algorithm used to generate these noise processes is found in appendix A.
Lastly in section 2.4 we will introduce the results obtained by Tayebirad et al. who already studied the system analyzed in this work. A more detailed discussion of these results will follow in section 4.3.

**Chapter 3:** In order to understand the influence of the noise on the system under consideration, we will first need to understand how the system behaves in the absence of noise. This chapter will therefore analyze the Wannier-Stark system in the presence of a second lattice that is *not* driven by noise but simply moves with

a constant velocity $\beta$. Since we assume this second lattice to have a lattice constant different from the one of the original Wannier-Stark problem, this will be called the *bichromatic tilted lattice system* or the *bichromatic Wannier-Stark system*.
In the first section of this chapter we will explain why this system is relevant to our understanding of the full noise-driven system that we want to study in this thesis.
In section 3.2 we introduce the bichromatic Wannier-Stark system and give a qualitative estimate of its behavior. Based on a simplified model of the system, this qualitative estimate is then refined into more quantitative predictions in section 3.3.
In section 3.4 we discuss the results obtained through numerical simulations of the noise-less bichromatic Wannier-Stark system. These results are then compared to the predictions made in section 3.2 and 3.3. While we find that the quantitative predictions cannot accurately describe the systems behavior, there is a good qualitative agreement with the model.

**Chapter 4:** In this chapter the main results of this thesis are presented. The focus is a better understanding of the behavior of the noise-driven bichromatic Wannier-Stark system.
In Section 4.1 we present an approach that uses the result from chapter 3 to model the influence of *slow noise* on the bichromatic Wannier-Stark system. We discuss the predictions derived through this approach and give a qualitative estimate on how the effects of *fast noise* will differ from these predictions.
In order to understand the noise-driven bichromatic Wannier-Stark system extensive numerical simulations were performed. While the algorithm used for the numerical simulations of the Schrödinger equation is presented in appendix B, the details of the simulations are explained in section 4.2. To this end we show how the initial state of the simulations is set up and define how the observable is measured.
In section 4.3 we discuss the results of the numerical simulations and compare them to the model introduced in section 4.1. We will observe that the model, even though not accurate for very fast noise can explain the influence of slow noise very well. We furthermore discuss how this model explains the effects previously observed by Tayebirad et al. (see section 2.4).

**Chapter 5:** In this chapter we will give a short recapitulation of the results obtained in chapter 3 and 4. We will moreover discuss interesting directions for further research and applications that could be based on the results of this thesis.

# 2 Preliminaries

## 2.1 Bose-Einstein Condensates and Optical Lattices

While the existence of Bose-Einstein condensates was already predicted at the beginning of the 20th century [9, 33], it took seventy more years to finally observe them in an experiment [3]. Named after the two physicists who first calculated its properties, this new state of matter should form for any weakly interacting Bosonic gas at low enough temperatures.

All particles that are part of such a condensate occupy the same quantum-mechanical state of the system. This is caused by the fact that the number of thermally available excited states diminishes rapidly for low temperatures. While we would of course expect that in a system at temperature $T = 0$, all particles are found in the ground state, we would naively assume that at a finite temperature only a diminishing fraction of all particles are found in this state. One can however calculate that for a non-interacting Bose-gas there exists a finite temperature $T_{crit}$, at which the sum over the expected occupation values of all excited states become too small to hold all particles. Below this temperature a finite fraction of all particles is therefore found in the ground state of the system. These particles thus all occupy the same state and form the Bose-Einstein condensate.

For a non-interacting Bose-gas, the temperature $T_{crit}$ at which this condensation happens can be calculated using only the density of states of the system and the Bose-Einstein distribution. This calculation is found in many textbooks on statistical physics, for example the book of Fließbach [12, Chapter 31]. At this transition temperature, the de Broglie wavelength of a thermally excited particle of a Bose-gas becomes comparable to the interparticle distance, giving another intuitive meaning to the condensation process. For realistic experimental systems with a particle density of $10^{13} - 10^{15} \frac{\text{atoms}}{\text{cm}^3}$ this corresponds to a critical temperature in the order of $10^{-7}$K [29].

Since all particles in the Bose-Einstein condensate occupy the same state, their wavefunction is identical. It is therefore possible to describe the whole Bose-Einstein condensate through this common wavefunction. The fact that a large number of particles is described by a coherent wavefunction allows one to observe quantum mechanical effects on macroscopic scales.

If the particles in the condensate are not interacting with each other, their com-

mon wavefunction is governed by the single-particle Schrödinger equation

$$i\hbar\partial_t\psi = -\frac{1}{2}\frac{\hbar^2\nabla^2}{2M}\psi + V(x)\psi. \tag{2.1}$$

While it is possible to keep the interactions between cold Bosonic atoms minimal through means of a Feshbach resonance [29], any experimental realization of a Bose-Einstein condensate will show interactions between the atoms in the condensate. In the low density limit, these interactions can be described using a mean-field approach known as Gross–Pitaevskii equation [29]. In this approach, the local potential is modified by the condensate density due to interactions between the atoms of the condensate, leading to the nonlinear Schrödinger equation

$$i\hbar\partial_t\psi = -\frac{1}{2}\frac{\hbar^2\nabla^2}{2M}\psi + V(x)\psi + gN_0|\psi|^2\psi, \tag{2.2}$$

where $N_0$ is the total number of atoms in the condensate and the term $g$ describes the nature and strength of the interaction. For positive values of $g$, the interaction is repulsive while for negative values of $g$ it is attractive.

In experiments, the potential term $V(x)$ in the linear (2.1) or nonlinear Schrödinger equation (2.2) can be controlled by various means, for example magneto-optical traps [7]. In this work we are however mainly interested in optical lattice potentials. These potentials are created by superimposing two counter-propagating but coherent laser light beams with a frequency close to an atomic resonance. Due to interference this results in a standing wave with nodes where the light interferes destructively and anti-nodes where the light interferes constructively. Atoms that are located at the nodes of this standing wave do therefore not experience any effect. Away from those nodes the energy states of the neutral atoms are, however, shifted due to an induced dipole moment. A detailed derivation of the resulting potential can be found in an article of Fischer and Raizen [11, Chapter 8]. We will skip the detailed treatment of this problem and only quote the resulting Hamiltonian

$$H = -\frac{\hbar^2\nabla^2}{2M} + V_0\cos\left(2\frac{2\pi x}{\lambda} - \phi(t)\right). \tag{2.3}$$

This expression is derived for two laser light beams with wavelength $\lambda$ that propagate in the $x$-direction. In order to simplify the expression we will define a new wave number $k = 4\pi/\lambda$ such that the potential term can be written as $V_0\cos(kx - \phi(t))$. The amplitude $V_0$ of the lattice potential depends on the intensity of the laser light and on how far the laser frequency is detuned from the atomic resonance [11, Chapter 8]. The phase shift $\phi(t)$ depends on the relative phase of the two superimposed laser light beams.

For a realization of the Wannier-Stark discussed in section 2.2, we also like to apply a static force $F$ to the whole Bose-Einstein condensate, thereby tilting the

optical lattice. This static force can be easily introduced into the optical lattice by making use of the time-dependent phase shift $\phi(t)$ in equation (2.3). Setting the phase shift to $\phi(t) = k\tilde{\phi}(t) - \frac{Fkt^2}{M}$ and applying a unitary transform allows one to write the Hamiltonian (2.3) in an accelerated frame of reference:

$$H = -\frac{\hbar^2\nabla^2}{2M} + V_0 \cos\left(k(x - \tilde{\phi}(t)\right) - Fx. \tag{2.4}$$

This so-called Wannier-Stark Hamiltonian will be studied in the following chapter.

## 2.2 Wavefunctions in Tilted Periodic Potentials: Avoided Crossings and Landau-Zener Transitions

In this section, we will demonstrate how the presence of a periodic lattice potential leads to the emergence of an energy band structure and how tunneling between these bands can be described. Starting with the Schrödinger equation in simplified units, we determine the effect of the lattice on the momentum eigenstates. Using this knowledge the emerging bandstructure is discussed. To better understand the influence of a static force on the transport properties of the system, we will use a Landau Zener model to describe the system near the bandgaps. Lastly the limitations of this Landau-Zener approximation are discussed.

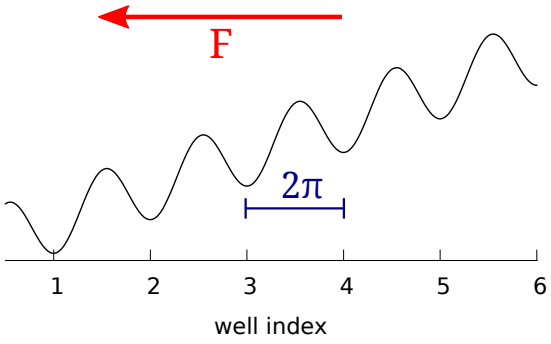


Figure 2.1: The tilted periodic lattice, with lattice constant $d_l = 2\pi$ and Stark Force F

### Band Structure in the Presence of a sinusoidal Lattice

The Schrödinger equation introduced in the previous section accurately describe the behavior of cold, non-interacting atoms in an optical lattice. In order to make the following calculations , we will introduce a new set of units. Starting with the full Schrödinger equation for the Wannier-Stark problem

$$i\hbar\partial_t\psi = \left(-\frac{\hbar^2}{2M}\partial_x^2 + V\sin(2k_l x) - Fx\right)\psi \tag{2.5}$$

and substituting $\tilde{x} = 2xk_l$ results in

$$i\hbar\partial_t\psi = \left(-4\frac{k_l^2\hbar^2}{2M}\partial_{\tilde{x}}^2 + V\sin(\tilde{x}) - \frac{F}{2k_l}\tilde{x}\right)\psi. \tag{2.6}$$

In order to remove the prefactor of the kinetic term and all occurrences of $\hbar$, we also renormalize the time scale by introducing $\tilde{t} = t\frac{1}{\hbar}4\frac{\hbar^2k_l^2}{M}$. All the remaining

factors can be absorbed by using rescaled values for $V$ and $F$. The simplified Schrödinger equation thus reads

$$i\partial_{\tilde{t}}\psi = \left(-\frac{1}{2}\partial_{\tilde{x}}^2 + V_0\sin(\tilde{x}) - F_0\tilde{x}\right)\psi, \tag{2.7}$$

where

$$\begin{aligned} V_0 &= V\frac{M}{4\hbar^2 k_l^2} = \frac{V}{8E_{rec}}, & \tilde{x} &= 2xk_l, \\ F_0 &= F\frac{M}{8\hbar^2 k_l^3} = \frac{F\lambda_l}{16\pi E_{rec}}, & \tilde{t} &= t\frac{1}{\hbar}4\frac{\hbar^2 k_l^2}{M} = t\frac{8E_{rec}}{\hbar}. \end{aligned} \tag{2.8}$$

The recoil energy $E_{rec}$ is defined as the kinetic energy an atom of the condensate would gain from absorbing a photon from the laser beam:

$$E_{rec} = \frac{(\hbar k_l)^2}{2M} = \frac{\hbar^2 k_l^2}{2M} \tag{2.9}$$

and the laser wavelength $\lambda_l$ is defined as $\lambda_l = \frac{2\pi}{k_l}$. Unless stated otherwise, this new set of units will be used throughout this work and hence we drop the tilde symbol over $x$ and $t$.

Now that the Schrödinger equation has been brought into a neater form, we would like to better understand the effect of the static force $F_0$. Let us consider a transformed wavefunction $\tilde{\psi} = e^{iF_0tx}\psi$ and examine how it is affected by the Schrödinger equation. The transformation is equivalent to a momentum boost $\tilde{p} = p + Ft$ and it is thus not surprising that it results in

$$\begin{aligned} e^{iF_0tx}\left(i\partial_t\psi - F_0x\psi\right) =& e^{-iF_0tx}\left(-\frac{1}{2}\partial_x^2\psi - iF_0t\partial_x\psi + \frac{1}{2}F_0^2t^2\psi\right) + \\ & \left(V_0\sin(x) - F_0x\right)\tilde{\psi} \end{aligned} \tag{2.10}$$

$$\Rightarrow \quad i\partial_t\psi = \frac{1}{2}\left(-i\partial_x + F_0t\right)^2\psi + V_0\sin(x)\psi, \tag{2.11}$$

where we divided by $e^{iF_0tx}$ to get the final result.

To understand how the dynamics of the system is influenced by the sinusoidal lattice, it is instructive to rewrite the Hamiltonian in the momentum basis. As the kinetic term is already written in terms of the momentum operator $-i\partial_x$, it is only necessary to investigate the effect on the second term of the right hand side

of (2.11):

$$\begin{aligned}
V_0 \sin(x) =& \int_{p,p'} |p'\rangle\langle p'|\, V_0 \sin(x)\, |p\rangle\langle p|\, dp dp' \\
=& V_0 \int_{p,p'} \int_x |p'\rangle e^{-ip'x} \frac{e^{-ix} - e^{+ix}}{2} e^{ipx} \langle p|\, dx dp dp' \\
=& \frac{V_0}{2} \int_{p,p'} \int_x |p'\rangle \left( e^{i(p+1-p')x} - e^{i(p-1-p')x} \right) \langle p|\, dx dp dp' \\
=& \frac{V_0}{2} \int_{p,p'} |p'\rangle \left( \delta(p+1-p') - \delta(p-1-p') \right) \langle p|\, dp dp' \\
=& \frac{V_0}{2} \int_p \left( |p+1\rangle\langle p| - |p\rangle\langle p+1| \right)\, dp.
\end{aligned} \tag{2.12}$$

This term does only couple momentum eigenstates with a difference in momentum $p$ of exactly one. As the kinetic term of the equation (2.11) does not couple states with different momenta, states with a non-integer difference in momentum are not coupled at all. Writing the momentum $p$ as

$$\begin{aligned}
p = z + q \qquad & z \in \mathbb{Z} \\
& q \in [-0.5, 0.5) \subset \mathbb{R}
\end{aligned} \tag{2.13}$$

allows one to write the Schrödinger equation in a form that shows this restriction more clearly:

$$i\partial_t \Psi(q,z) = (q + z + F_0 t)^2 \Psi(q,z) + \frac{V_0}{2} \left[ \Psi(q,z+1) - \Psi(q,z-1) \right]. \tag{2.14}$$

In this notation, only states with the same $q$ are coupled and no transitions between states with different $q$ are therefore possible. If the system is prepared in a state with a fixed value of $q$, it can thus only access a countable set $\{z\}$ of states with the same $q$.

Let us for now ignore the time-dependent term $F_0 t$ and focus on the energy levels of the system at a fixed time. We will call the states with $q$ and $z$ fixed the *diabatic states* $\Psi(q,z)$ of the system. Their energies are identical to those of a free particle with momentum $q + z$ and can be seen in figure 2.2a as dashed lines. Each one of the states $\Psi(q,z)$ can be seen as a parabola in $q$ centered at $-z$. The eigenstates of the system are called the *adiabatic states*[1] and their energies are shown as solid lines in figure 2.2a. As the states with different $z$ are coupled through the lattice term, the eigenstates are in general not identical to the diabatic states. Unlike the diabatic states, whose energy levels cross for certain values of $q$, the adiabatic states show *avoided crossings*. The adiabatic states can therefore be divided into different *bands* which are seperated by *bandgaps* [1].

-

[1] In order to find the eigenstates, one has to solve the so-called Mathieu equation. While these solutions are known, they cannot be easily expressed analytically.

## Avoided Crossings in the Landau-Zener Approximation

In the present work we will be mostly interested in the tunneling from the ground band up to higher bands. To understand the behavior of the system close to the bandgaps, consider the general case of two coupled quantum mechanical states A and B whose energies change as a result of an external parameter. If the state A is forced through an avoided crossing with state B through the change of the external parameter, any wavefunction that is initially prepared in the state A will afterwards be in a superposition of the two states. The adiabatic theorem helps us understand, what will happen in the limiting cases of very slowly or rapidly changing momentum. If the external parameter changes very rapidly, the dynamics of the system is too slow to effect any change of the wavefunction, meaning that the system stays in the same diabatic state. If on the other hand the external parameter changes very slowly, the system will remain in the same adiabatic state. In our system the change in the parameter $q$ is caused by the static force $F$. A strong force means that the system will remain in the diabatic state $\Psi(q,z)$ it was initially prepared in, translating into complete tunneling into the higher band at bandgaps. For a very weak force, the system does stay in its adiabatic state, leaving it confined to the band it was prepared in.

Placed in the lowest band, a momentum eigenstate will continuously accelerate until it hits a bandgap. There a part of it will be reflected and thus remain in the ground band while a part of it will tunnel through the bandgap to the next band. The probability to remain in the groundband remains nearly constant while $-0.5 < q < 0.5$, but drops every time an avoided crossing is reached (see figure 2.3b). This happens once per Bloch period $T_{\text{Bloch}}$:

$$T_{\text{Bloch}} = \frac{1}{F_0} \qquad \nu_{\text{Bloch}} = \frac{1}{T_{\text{Bloch}}} = F_0. \tag{2.15}$$

To better understand the behavior of the system close to the bandgaps, we look at the Landau-Zener approximation of the system at the avoided crossings. Writing the Schrödinger equation (2.14) for a fixed $q$ in matrix form reads

$$i\partial_t \Psi(q,z) = \frac{1}{2} \begin{pmatrix} \ddots & V_0 & 0 & 0 & 0 \\ V_0 & (q-1+F_0t)^2 & V_0 & 0 & 0 \\ 0 & V_0 & (q+F_0t)^2 & V_0 & 0 \\ 0 & 0 & V_0 & (q+1+F_0t)^2 & V_0 \\ 0 & 0 & 0 & V_0 & \ddots \end{pmatrix} \Psi(q,z). \tag{2.16}$$

The dynamics close to a bandgap can be approximated by only considering the two states involved locally in the avoided crossing. For the gap between the two lowest bands at $q = 0.5$, these would be the states $\Psi(q,0)$ and $\Psi(q,-1)$. Let us ignore all terms that couple these states to the rest of the system and restrict the

Hamiltonian to the part highlighted in (2.16)

$$H_{LZ} = \frac{1}{2}\begin{pmatrix} [(q + F_0 t) - 1]^2 & V_0 \\ V_0 & [q + F_0 t]^2 \end{pmatrix}$$
$$= \frac{1}{2}\begin{pmatrix} (q + F_0 t)^2 + 1 - 2(q + F_0 t) & V_0 \\ V_0 & (q + F_0 t)^2 \end{pmatrix}.$$

Setting $q = 0.5$ and changing the energy scale by subtracting $(q + F_0 t)^2 + F_0 t$ from the diagonal transforms this into

$$H_{LZ} = \frac{1}{2}\begin{pmatrix} -F_0 t & V_0 \\ V_0 & F_0 t \end{pmatrix}. \tag{2.17}$$

This reduced Hamiltonian is the well-known Landau-Zener model. The energy levels of the Landau-Zener model can be seen in figure 2.2b, where dashed lines again denote the diabatic states whereas solid lines represent the adiabatic states. The energies of the adiabatic states are

$$E^{\pm}_{\text{adiabatic}} = \pm\frac{1}{2}\sqrt{F_0 t^2 + V_0^2}, \tag{2.18}$$

leading to a bandgap of width $V_0$. An exact solution for the asymptotic tunneling probabilities was published by Landau and Zener ([22, 46]): Assuming the system is prepared in one of the diabatic states at $t = -\infty$, this solution predicts that at $t = +\infty$, the probability that the system is still in the same diabatic state equals

$$P_{LZ} = \exp\left(-\pi\frac{V_0^2}{2F_0}\right). \tag{2.19}$$

A more concise proof of this than given in the original papers can be found in [45].

The presence of the bandgaps can be represented as barriers in momentum space. An accelerated state hitting one of the barriers at $p = 0.5$ will only partially tunnel through it with probability $P_{\text{tunnel}} = P_{LZ}$. Another part of it will be reflected with $P_{\text{reflection}} = 1 - P_{LZ}$. The reflected part of the wavefunction is transported to the momentum $p = -0.5$ (visualized in figure 2.4). A part of the wavefunction will therefore be trapped within the barriers. This corresponds to the part of the wavefunction that remains in the ground band.

## Limits of the Landau-Zener Approximation

It should be kept in mind that this approximation is only strictly true for the gap between the first and the second gap. The higher bandgaps result from coupling through an intermediate state and are therefore somewhat more complicated to

deal with. However, as the width decreases between higher bands, the tunneling through these gaps is exponentially enhanced when compared to the first gap. As an example the width of the second bandgap scales as $V_0^2/2$ for $V_0 \ll 1$, meaning that for small $V_0$, the probability to tunnel from the second to the third band is exponentially enhanced. Subsequent bandgaps scale with even higher powers of $V_0$ [28]. For small $V_0$, all tunneling probabilities between higher bands can therefore be approximated as $P_{LZ}^{\{n\}} \approx 1$.

While the Landau-Zener formula (2.19) accurately predicts the tunneling probabilities for the reduced Hamiltonian, it cannot account for all effects that occur in the full system. In any real system the transition takes place during a finite time, whereas the Landau-Zener formula is only correct for transition that are given an infinite amount of time. To understand how a finite timescale influences the transition process, it is instructive to look at the time-dependence of the adiabatic tunneling probabilities (see figure 2.5). While there are oscillations up to larger values of $t$, the probability changes most drastically in a small region around $t = 0$. A more thorough analytical and numerical investigation by Vitanov ([41]) finds that there are indeed two relevant timescales of the transmission. There is the *jump time* $\tau_{jump}$, the time needed for $P_{surv}$ to reaching its asymptotic value for the first time. Furthermore there is the *relaxation time* $\tau_{relax}$ which describes the time needed for the oscillations of $P_{surv}$ to be damped to a sufficiently small value.

In the present work the more important timescale is the jump time. While it cannot be ruled out that the oscillations around the asymptotic value influence subsequent avoided crossings, the jump time gives a lower bound for the separation needed for two successive Landau-Zener transitions to be considered independent. For the range of parameters studied in this work, Vitanov ([41]) finds the jump time to be

$$\tau_{jump} = \frac{V_0}{\sqrt{2F_0}}. \tag{2.20}$$

The time between two avoided crossings in the full system (2.16) is the Bloch time $T_{Bloch}$. The Landau-Zener formula is only applicable if the jump time is smaller than $T_{Bloch}$:

$$\tau_{jump} \leqslant T_{Bloch} \Leftrightarrow F_0 \leqslant \frac{2}{V_0^2}. \tag{2.21}$$

Rigorously defining the two timescales in a meaningful way is not as straightforward as it seems and the results (2.21) should therefore be seen more as a guideline than a strict condition [47].

## Multiple Crossings: RET and Multilevel Landau-Zener

An effect not considered in the Landau-Zener picture is *resonantly enhanced tunneling* (RET). This effect is due to interference between the part of the wavefunc-

tion that has escaped to the second, but not the third band and the part of the wavefunction that remains in the first band. As there is a q-dependent energy difference between the two bands, a phase difference of

$$\Phi = \int_0^{T_{\text{Bloch}}} i\big[E_2(q(t)) - E_1(q(t))\big]dt \tag{2.22}$$

is accumulated up during each Bloch period. Depending on this phase difference, tunneling can be either enhanced or suppressed [25].

During the last decade, there has also been a plethora of research on the *multi-state Landau-Zener* problem. In this problem, a crossing of more than two energy levels occurs within a short time such that avoided crossings overlap. In spite of the complexity of the problem[2], some interesting analytical results have been found:

- The *no-go-theorem* states that certain transitions are completely forbidden. These transitions are those that would also be forbidden in the approximation where the problem is treated as succession of separate Landau-Zener events. This means for example that in figure 2.6 for a sweep from the left to the right (q increases in time), no transition from the lowest level on the left to the highest level on the right is possible [36].

- Certain elements of the transition matrix can be found by simply treating the problem as a series of unconnected Landau-Zener events. Among these is the probability to remain in the diabatic state with the highest slope [4].

In certain situations, the additional effects brought into play by multiple level crossings are therefore negligible and the multilevel Landau-Zener problem can be simply treated as a succession of individual Landau-Zener events between different diabatic states.

[2]Due to the fact that a number of interference terms similar to the one noted in (2.22) appear, even treating the problem as a succession of separate Landau-Zener events quickly gets very complicated.

## 2.3 Stochastic Differential Equations, Noise Processes and Harmonic Noise

The history of stochastic differential equations in physics goes back to Einsteins solution of the Brownian Motion problem [8]. Since then the formalism for treating these problems has evolved considerably and today it has found manifold application in such different fields as biology, economics, chemistry and solid state physics.

Stochastic differential equations are differential equations influenced by one or more stochastic processes. As such their solutions themselves are necessarily also a stochastic process.

Let us consider stochastic differential equation that follow the Langevin equation

$$\dot{y}(t) = f\big(y,t\big) + g\big(y,t\big)\xi(t) \tag{2.23}$$

with a noise term $\xi(t)$. These differential equations can be seen as a map of the original stochastic process $\xi(t)$ onto a new stochastic process $y(t)$. In this work, we will always defined $\xi(t)$ as a zero mean Gaussian white noise term with the correlation function

$$\langle \xi(t)\xi(t')\rangle = \delta(t-t'). \tag{2.24}$$

This correlation function tells us two things: there is *no correlation* between the $\xi(t)$ at two different times and $\xi(t)$ has *infinite variance*. Since $\xi(t)$ has infinite variance, it cannot be understood as an ordinary noise variable. Its meaning in the stochastic differential equation becomes clearer when observing the integral $W(t)$ over the white noise process:

$$W(t) = \int_0^t \xi(t')dt'. \tag{2.25}$$

$W(t)$ has the variance

$$\langle W(t)^2\rangle = \left\langle \int_0^t \int_0^t \xi(t_1)\xi(t_2)dt_1'dt_2' \right\rangle = \int_0^t dt_1' = t. \tag{2.26}$$

Calculating the higher momenta of the so-called Wiener process $W(t)$ reveals that it follows a Gaussian distribution with standard deviation $\sigma = \sqrt{t}$. It can therefore be considered a diffusion process. An analogy to help understand this is a random walk is interpreting the integral (2.25) as a random walk, that adds up an infinite number of steps $\xi(t)$.

Integrating the stochastic differential equation (2.23) through a Riemann or Lebesgue integral is not possible because $\xi(t)$ and hence the whole right side of the equation does not assume a finite value. One therefore needs to come up

with a definition that incorporates the noise term in a more sensible way. This is done by putting the Wiener process $W(t)$ at the core of the integration. The *Ito stochastic integral* over a function $f(t)$ using Wiener process $W(t)$ is defined as a kind of Stieltjes integral:

$$\int_0^t f(t')\xi(t')dt' = \int_0^t f(t')dW(t') \tag{2.27}$$

$$= \lim_{N\to\infty} \left\{ \sum_{i=1}^{N} f(t_{i-1})[W(t_i) - W(t_{i-1})] \right\}. \tag{2.28}$$

While this definition at first seems similar to the Riemann integral, its implications on the resulting calculus are not straightforward[3]. A reader interested in more information about this topic is referred to the book of Gardiner [17].

In order to discuss the noise processes which will be used in this work let us first some of their properties that we can use to characterize them. A noise process initially prepared in a state $y(0)$ will undergo a stochastic evolution. Its value $y(t)$ at a later time $t > 0$ will therefore obey a distribution $P(y, y_0)_t dy$. For many noise processes, this distribution function $P(y, y_0)_t dy$ approaches a *static equilibrium distribution* $P_{equ}(y)dy$ for $t \to \infty$. This means that in this limit, the distribution does neither depend on $t$ nor the initial state $y_0$ anymore. For a noise process prepared with initial states $y_0$ according to this distribution, the probability density for $y(t)$ will always be given by $P_{equ}(y)dy$. This static equilibrium probability density therefore describes the distribution for $y(t)$ of a noise process for which no information about previous states is known.

While the equilibrium distribution of a noise process tells us about its static properties, it does not convey any information about the dynamics of the process. How the noise process influences other systems is however usually also determined by the way $y(t)$ changes over time. An important property incorporating this time-dependence is the *two-time correlation function* $R(h) = \langle y(t_0)y(t_0 + h)\rangle$ and the related power spectrum. For $h = 0$, the correlation function is equal to the variance of the noise process $R(0) = \langle y(t)^2\rangle$. For very long times $h$, the correlation function $R(h \to \infty)$ will converge to zero if the noise process

The *power spectrum* is defined as the Fourier transform of the correlation function

$$S(\omega) = \int_{-\infty}^{+\infty} \langle y(0)y(t')\rangle e^{-2i\pi\omega t'} dt'. \tag{2.29}$$

Through the Wiener-Khinchin theorem this spectrum is related to the absolute square of the Fourier transform of the noise process. For a system only responding to a signal of certain frequencies, the power spectrum can thus tell us how

[3]One should also keep in mind that equation (2.28) is not the only definition one can use for stochastic integrals. Using another definition like for example the Stratonovich integral will change the properties of the noise process $W(t)$ as well as the solutions of stochastic differential equations.

strongly this system should be influenced by the noise process. While the power spectrum of the white noise process is completely flat, the noise processes used in this work feature spectra with maxima at specific frequencies as shown in figure 2.7b and 2.7d.

Using the definition of stochastic integrals, we can now proceed to define and analyze the noise processes we will study in chapter 4 of this work: the *harmonic noise* as well as the *exponentially correlated noise*.

Let us first consider the exponentially correlated noise. This noise, also known as Ornstein-Uhlenbeck process is defined by the Langevin equation

$$\dot{\phi}(t) = -\Gamma\phi(t) + \sqrt{2T}\xi(t). \tag{2.30}$$

This equation can be thought of as representing the velocity of a particle undergoing Brownian motion in a one-dimensional system. A randomly fluctuating force $\sqrt{2T}\xi(t)$ accelerates the particle, but the motion is damped by a viscous drag term $\Gamma\phi(t)$. In figure 2.7a, a realization of this noise process is plotted.

The equilibrium distribution of this process is (see [17, chapter 4.4.4])

$$P_{equ}(\phi)d\phi = \frac{1}{\sqrt{2\pi T}} e^{-\frac{\phi^2}{2T}}. \tag{2.31}$$

This defines a zero-mean Gaussian distribution with variance $T$. The two-time correlation function is given by

$$\langle \phi(t_0)\phi(t_0+h)\rangle = Te^{-\Gamma|h|}. \tag{2.32}$$

The correlation decays with a characteristic time of $1/\Gamma$ which is of course the reason for the name of the noise process. The resulting power spectrum has the form of a Lorentzian function

$$S(\omega) = \frac{2\Gamma T}{\omega^2 + \Gamma^2}. \tag{2.33}$$

This spectrum is peaked at $\omega = 0$ with a full width at half maximum of $\Gamma$ (see figure 2.7b). The exponentially correlated noise can thus be seen as a white noise process subject to a low-pass filter.

The harmonic noise process follows the Langevin equation

$$\begin{aligned} \dot{\phi} &= \nu \\ \dot{\nu} &= -2\Gamma\nu - \omega_0^2\phi + \sqrt{4\Gamma T}\xi(t). \end{aligned} \tag{2.34}$$

Similar to the exponentially correlated noise, it can be imagined as a particle undergoing Brownian motion, but this time in the presence of an harmonic potential. If this harmonic potential is sufficiently relaxed, one would expect this process to approach the free case described by the exponentially correlated noise process. In the limit $\omega_0 \to 0$, the equation (2.34) indeed turns into (2.30). We

therefore expect the properties of $\nu$ to approach those of the exponentially correlated noise in this limiting case.

In figure 2.7c we can see that the noise variables undergo an oscillatory motion. Due to the similarity to the harmonic oscillator, $\phi(t)$ and $\nu(t)$ have a phase difference of $\pi/4$, but otherwise perform a similar motion. It should however be noted that the signal $\phi(t)$ is much smoother than $\nu(t)$ or the exponentially correlated noise visible in figure 2.7a. This is due to the fact that integrating turns the discontinuous $\nu$ into a continuous process.

The equilibrium distribution of the harmonic noise process is a bivariate Gaussian distribution (see [42])

$$P(\phi,\nu)d\phi d\nu = \frac{\omega_0}{2\pi T} e^{-\frac{\phi^2}{2T}\omega_0^2} e^{-\frac{\nu^2}{2T}}. \tag{2.35}$$

In this distribution, the two variables $\phi$ and $\nu$ of the noise process are completely independent and their variances are

$$\langle \phi^2 \rangle = \frac{T}{\omega_0} \tag{2.36}$$

$$\langle \nu^2 \rangle = T. \tag{2.37}$$

The equilibrium distribution thus only differs from the exponentially correlated noise in the fact that it is two-dimensional, but it still follows a normal distribution. However when looking at the correlation function, the differences between both noise processes become clear. The correlation functions for the harmonic noise process are (see [42])

$$\begin{aligned}
\langle \phi(t)\phi(t+h) \rangle &= \frac{T}{\omega_0^2} e^{-\Gamma h} \left( \cos(\omega_1 h) + \frac{\Gamma}{\omega_1} \sin(\omega_1 h) \right) \\
\langle \nu(t)\nu(t+h) \rangle &= T e^{-\Gamma h} \left( \cos(\omega_1 h) + \frac{\Gamma}{\omega_1} \sin(\omega_1 h) \right) \\
\langle \nu(t)\phi(t+h) \rangle &= \frac{T}{\omega_1} e^{-\Gamma h} \sin(\omega_1 h),
\end{aligned} \tag{2.38}$$

where the frequency $\omega_1$ is defined as $\omega_1 = \sqrt{\omega_0^2 - 2\Gamma^2}$. The correlation function thus undergoes a similar decay as the exponentially correlated noise but additionally performs oscillations with the frequency $\omega_1$. This is exactly what one would expect from the damped harmonic oscillator which shows exactly the same behavior.

For $\sqrt{2}\Gamma > \omega_0$, the frequency $\omega_1$ is an imaginary number. Correspondingly to an overdamped harmonic oscillator, the oscillations in the correlations functions 2.38 vanish. This can be seen by writing an imaginary $\omega_1$ as $i\omega'$ with real $\omega'$ and noting that $\sin(i\omega' h) = i\sinh(\omega' h)$ as well as $\cos(i\omega' h) = \cosh(\omega' h)$. Neither sinh nor cosh show oscillatory behavior and all correlations thus decay without oscillations. The same is true for the aperiodic case which is reached for $\omega_1 = 0$.

The power spectrum of the harmonic noise process is also of Lorentzian shape and for $\phi(t)$ can be written as

$$S_\phi(\omega) = \frac{2\Gamma T}{\pi(4\Gamma^2\omega^2 + (\omega^2 - \omega_0^2)^2))}. \tag{2.39}$$

But unlike the exponentially correlated noise, it attains its maximum at $\omega_1$ which is in general not equal to zero (see figure 2.7d). The full-width half maximum of the peak can be approximated as $2\Gamma$ for small values of $\Gamma/\omega_0$. The harmonic noise can therefore be seen as band-pass filter that suppresses all frequencies except those close to $\omega_1$.

An interested reader can find the derivation of all these properties in [42] or [5].

## 2.4 A first Look at Noise-Influenced Tunneling in Optical Lattices

Chapters 3 and 4, which constitute the main part of this thesis, will be dedicated to analyzing a noise-influenced Wannier-Stark system previously studied by Tayebirad et al. [39]. In this section we will give a short overview over the motivation for studying this system and show the findings already made by Tayebirad et al. After having developed a framework for understanding this system in chapters 3 and 4, we will come back to these results and analyze them in a more detailed fashion.

The influence of noise on transitions in classical systems has received widespread attention because of the occurrence of interesting phenomena and its potential for applications in many different fields [24, 34, 37]. The phenomena of stochastical resonance, for example, has been studied extensively due to its relevance for the fields of biophysics and meteorology (see review article [16]).

While noise-influenced Landau-Zener transitions have also received attention in the literature [20, 19, 31, 30], the influence of noise on the Wannier-Stark problem has only been investigated recently [32].

Tayebirad et al. [39] studied such a noise-driven Wannier-Stark system by means of numeric calculations. They chose a Hamiltonian

$$H = -\frac{1}{2}\partial_x^2 + \gamma\frac{1}{2}V_0\sin(2kx) + \gamma\frac{1}{2}V_0\sin\left(2k'x + 2\phi(t)\right) + Fx \tag{2.40}$$

which incorporates the effect of two lattice potentials. The time-dependent phase $\phi(t)$ of the second lattice is given by a the harmonic noise process introduced in section 2.3. The effect of this can be imagined as the second lattice being "shaken around" by the noise process. Both lattice potentials are rescaled by a parameter $\gamma$ which is explained in [38] and [39]. For the short analysis made in this section, we will however ignore the effect of this parameter $\gamma$.

The influence of harmonic noise on quantum-mechanical problems has until now not received much attention. In classical systems it has, however, been shown that harmonic noise can enhance transition rates when compared to white or exponentially correlated noise [34]. One would therefore expect that its effect on the Wannier-Stark problem is a similar one.

As explained in section 2.2, the timescale of the Wannier-Stark problem is defined by the Bloch time $T_{\text{Bloch}} = 1/F$ and the associated Bloch frequency $\omega_{\text{Bloch}} = 2\pi/T_{\text{Bloch}}$. One would therefore expect to find interesting behavior if the system is driven by a noise process of a similar frequency. For $V_0 \ll 1$, the dynamics in the Wannier-Stark system are dominated by the Landau-Zener tunneling through the first band gap. We are therefore interested in how the tunneling from the ground band to the first band changes, when the system is driven by a noise process.

Using two lattice potentials at first glance seems to make the problem needlessly complex. The reason it is necessary however becomes clear once one considers how the system is affected if the noise term $\phi(t)$ fluctuates very rapidly.

In this limit, the second lattice term changes so rapidly that the system can only react to a time-averaged potential. This averaged potential can be written as an integral over all possible values for $\phi$, weighted with their equilibrium probability:

$$V_{avg} = \int_{-\infty}^{+\infty} V(x,\phi)P(\phi)d\phi \tag{2.41}$$

$$= \int_{-\infty}^{+\infty} \sin(2k'x + 2\phi)\frac{1}{\sqrt{2\pi\sigma^2}} e^{\frac{\phi^2}{2\sigma^2}} d\phi \tag{2.42}$$

$$= \exp(-2\sigma^2)\sin(2k'x). \tag{2.43}$$

For fast noise processes, the noise-driven lattice is therefore suppressed by a factor $\exp(-2\sigma^2)$, where $\sigma$ is the standard deviation of the noise process $\phi(t)$. If only the noise-driven lattice was present in the system, this suppression of the lattice potential would strongly change the dynamics of the system. The static lattice provides a reference system even in this limit of very fast noise.

While the survival probability in the ground band shows a step-like structure for the Wannier-Stark problem (see section 2.2), this property is lost in the presence of a second noise-driven lattice as can be seen in figure 2.8a. In order to analyze the influence of the noise parameters, Tayebirad et al. compared the survival probability in the ground band at a fixed time $t_0 = 6T_{Bloch}$ for different noise parameters. They found that the escape from the ground band was strongly influenced by the parameters of the harmonic noise process. Using a rescaled noise frequency

$$\omega' = \frac{\omega_0}{2\omega_{Bloch}}\sqrt{\langle\phi^2\rangle}\frac{k}{k'} \quad , \tag{2.44}$$

and fixing the variance $\langle\Phi^2\rangle$ of the noise process, the results of their investigation can be seen in figure 2.8b. For the parameters covered in their investigation, the escape from the ground band was maximized if this rescaled noise frequency assumed values close to unity. For frequencies close to this maximum, the decay rates of the system showed a universal behavior that did not depend on $\langle\Phi^2\rangle$ anymore.

A similar effect can be observed for a tilted bichromatic lattice system where the amplitude of the second lattice potential is driven by a harmonic noise process. The Hamiltonian of such a system can be written as

$$H = -\frac{1}{2}\partial_x^2 + \frac{1}{2}V_0\sin(2kx) + \frac{1}{2}\phi(t)\sin(2k'x) + Fx. \tag{2.45}$$

Numerical studies performed in the early phases of this diploma thesis show that this system shows a similar response to the frequency of the harmonic noise process as the one studied by Tayebirad et al. As shown in figure 2.9, we also observe a maximal escape rate from the ground band if the rescaled frequency of

the noise process is equal to one. It should however be noted that the behavior was less universal than the one observed by Tayebirad et al. and only visible for certain parameters of the system.

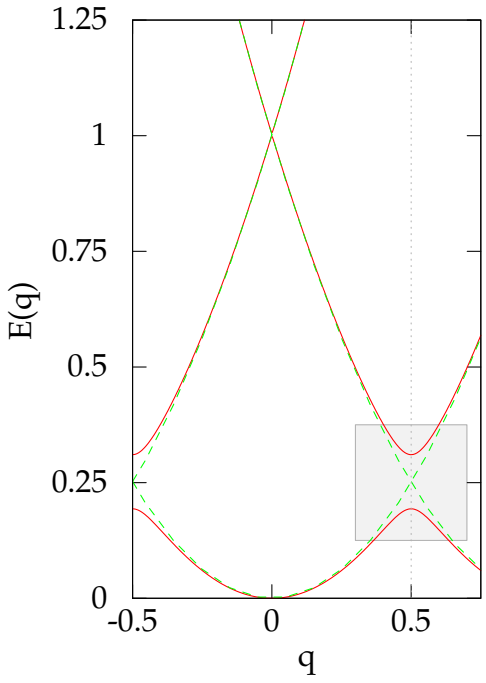


(a) The full system

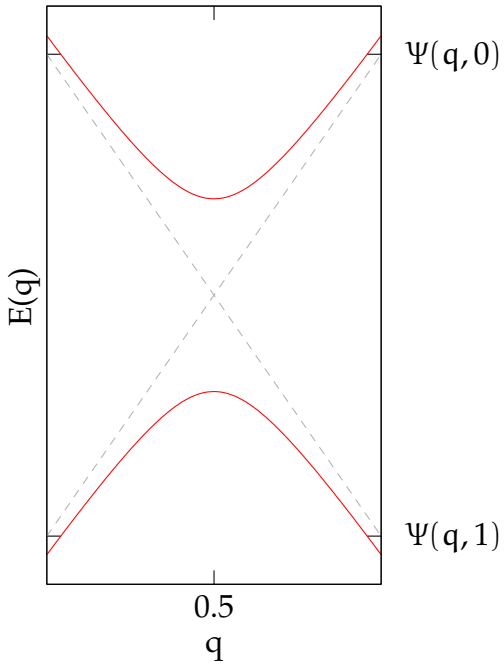


(b) Avoided Crossing in the Landau-Zener approximation

Figure 2.2: The coupling between the states leads to avoided crossings and the emergence of energy bands. The dotted states denote the energies for the free particle Hamiltonian. The solid line represents the eigenenergies of a system with a sinusiodal potential.

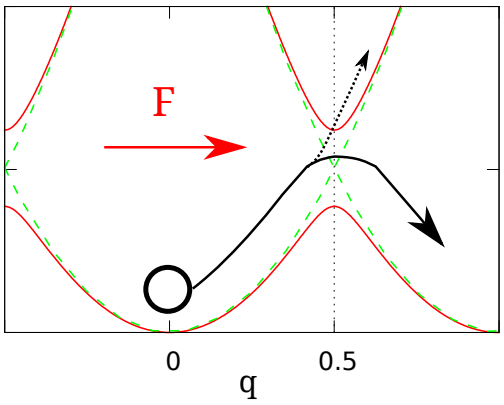


(a) State moving through bandgap

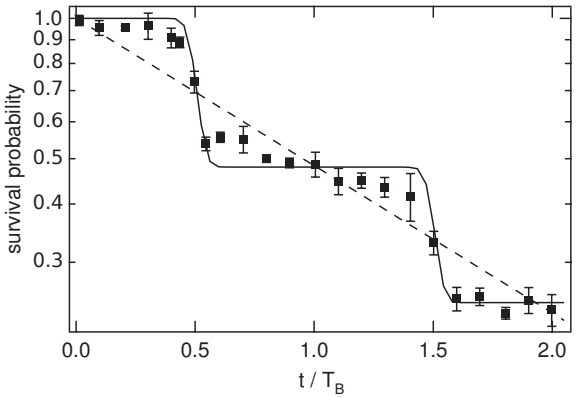


(b) Experimental data from [47] (Courtesy of the authors ©APS)

Figure 2.3: Decay of a state in the lowest band. While $|q| < 0.5$, the probability to stay in the band remains constant but drops every time a bandgap is encountered

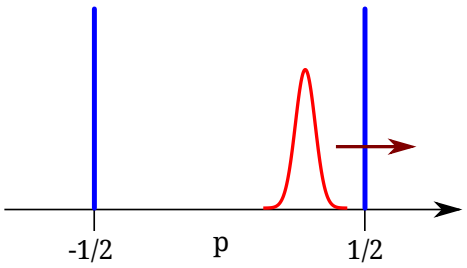


(a) Before hitting the barrier

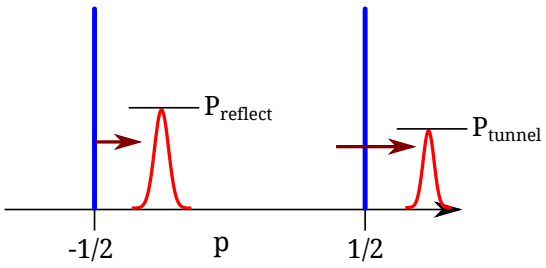


(b) After hitting the barrier

Figure 2.4: The Landau-Zener approximation can be represented as barriers in momentum space. When a state hits one of the barriers, only a part of it goes tunnels through this barrier. Another part is reflected by the barrier, which corresponds to a momentum change $\Delta p = -1$.

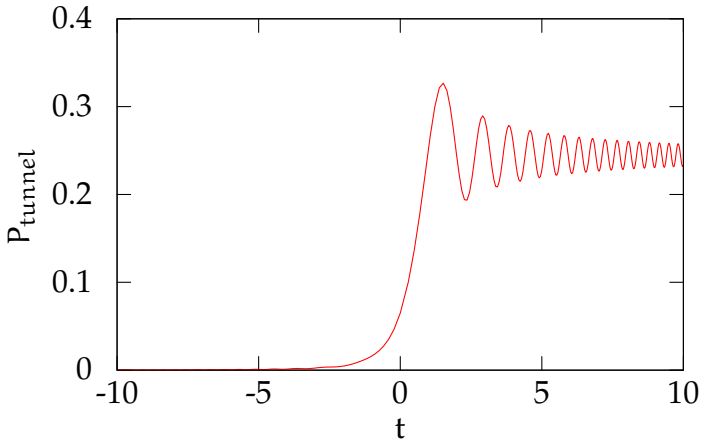


Figure 2.5: Probability to remain in the same diabatic Landau-Zener state plotted against time.

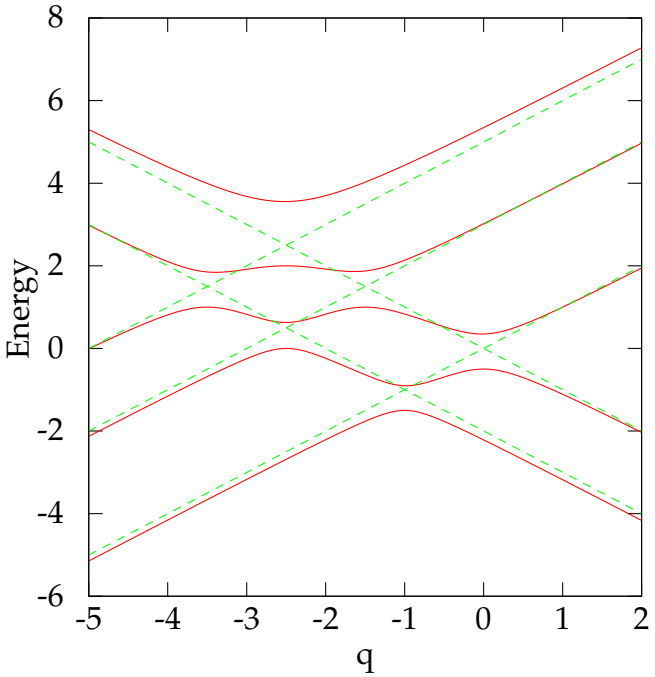


Figure 2.6: Landau-Zener crossing for multiple levels

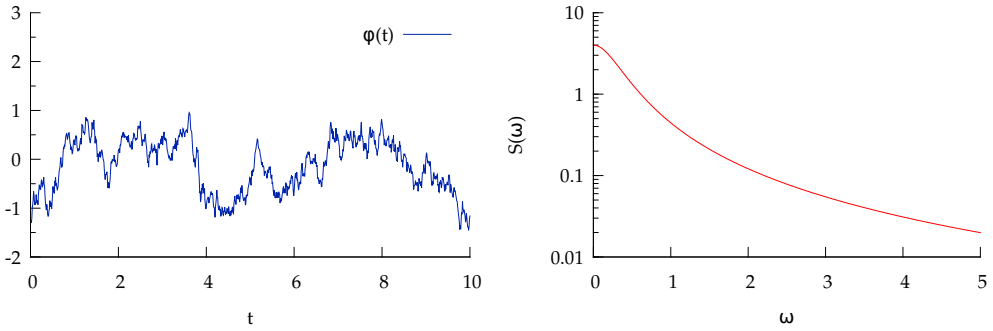


(a) Realization of Exponentially correlated noise

(b) Spectrum of Exponentially correlated noise

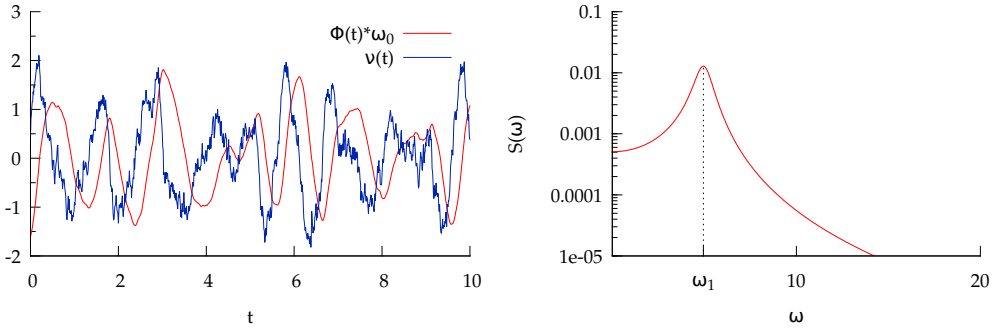


(c) Realization of harmonic noise

(d) Spectrum of harmonic noise variable $\phi(t)$

Figure 2.7: Properties of harmonic and exponentially correlated noise. For both noise processes the following parameters were chosen: $T = 1.0, \Gamma = 1.0, \omega_0 = 5.0$.

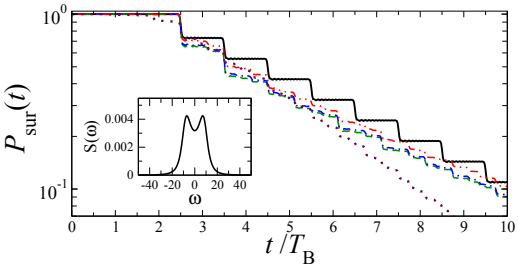


(a) The decay of the survival probability plotted against time for different noise parameters. The solid curve shows the decay for the noiseless monochromatic Wannier-Stark system.

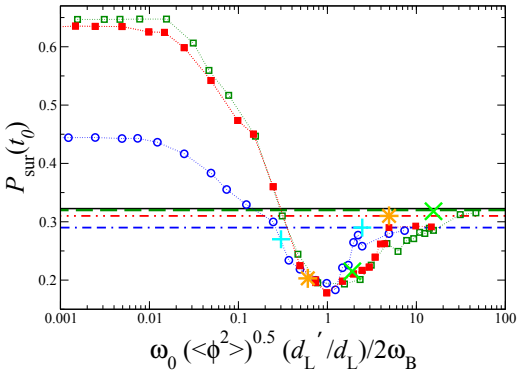


(b) The escape probability $P_{esc}$ after six Bloch periods plotted against the rescaled frequency of the noise process for fixed variances $\langle\phi^2\rangle$. The different colors correspond to different variances: $\langle\phi^2\rangle = 0.25$ (blue open circles), $\langle\phi^2\rangle = 1$ (red filled squares) and $\langle\phi^2\rangle = 10$ (green open squares)

Figure 2.8: Numerical data for system studied by Tayebirad et al. in [39] (Courtesy of the authors)

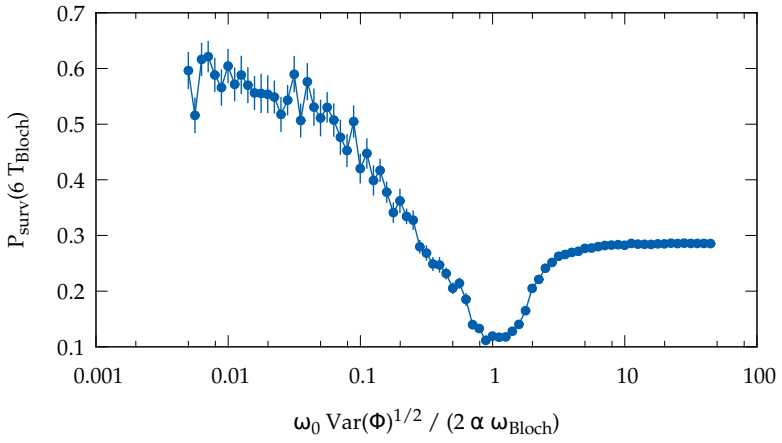


Figure 2.9: Influence of a second lattice with noise-driven amplitude on the decay rate $\gamma$. The parameters of the system are $F = \frac{1.146}{\pi 16}$, $V_0 = 2.5/16$, while the noise process used $\Gamma = 5.0$ and $T = 0.25$.

# 3 The influence of bichromatic Lattices on the Wannier Stark problem

While chapter 2 was used to introduce the concepts necessary to motivate this work to the reader, beginning with this chapter the new results attained in this diploma thesis will be presented.

The aim of this diploma thesis is to better understand the transport properties of noise-driven, bichromatic lattice systems like the one presented in section 2.4. The analysis of this systems is made complicated by the fact that the observed effects arise from an interplay between the bichromatic lattice and the driving by the noise process. In this chapter we will therefore present the findings in regard to bichromatic lattice systems in the absence of noise. The insight gained in this chapter will then help to better understand the noise-driven in chapter 4.

In section 3.2 we will first give a qualitative overview over the new effects occurring when a second lattice is introduced into the Wannier-Stark problem. Building upon these findings, we will build a model that approximately describes the transport properties in this bichromatic Wannier-Stark system in section 3.3. After this we will look at data from numerical simulations in order to evaluate the model from section 3.3 and the qualitative estimates from section 3.2. These quantitative numerical results will then be used in chapter 4 to partially explain the behavior of the noise-driven bichromatic system.

## 3.1 Relevance of the Noise-less Bichromatic Lattice System

The Hamiltonian of the noise-driven system we study can be written as

$$H = -\frac{1}{2}\partial_x + V_0 \sin(x) + V_1 \sin\left(\alpha(x - \phi(t))\right) - Fx, \tag{3.1}$$

where the time-dependent phase shift of the second lattice is defined by a noise process $\phi(t)$. If not stated otherwise, $\phi(t)$ represents a harmonic noise process as described in section 2.3.

In order to understand how the Wannier-Stark system is influenced by this additional, noise-driven lattice, we need to first understand the way the system is influenced by a second lattice in the absence of noise. Building upon the understanding of this noiseless system, we will be better prepared to interpret the results for the noise-driven system.

To this end we will first analyze the system defined by the Hamiltonian

$$H = -\frac{1}{2}\partial_x^2 + V_0 \sin(x) + V_1 \sin\left(\alpha(x - \beta t)\right) - Fx, \tag{3.2}$$

where the noise term has $\phi(t)$ has been replaced by a term $\beta t$, which is linear in time. Understanding the transport properties of this system will allow us to separate the effects in the full system that are caused by the stochastic properties of the noise from the ones that are due to the presence of a second moving lattice.

## 3.2 Bichromatic Lattices without Noise

In this Section we will investigate the effect of adding a second periodic lattice to the system. We start by considering a system subject to a static force and a single periodic potential, similar to the one studied in section 2.2. Instead of a static lattice with a period of $2\pi$ we will however investigate the dynamics of a lattice with period $\alpha 2\pi$ which is moving with velocity $\beta$. The Hamiltonian of this system reads

$$H = -\frac{1}{2}\partial_x^2 + V\sin\big(\alpha(x-\beta t)\big) + Fx. \tag{3.3}$$

For $\beta = 0$, an energy bandstructure with gaps at $p = \pm\alpha/2$ emerges[1]. The influence of the velocity $\beta$ can be understood by using a set of coordinates boosted with a velocity $\beta$[2]. This transforms the Schrödinger equation into

$$i\partial_t\psi = \left(\frac{1}{2}(\hat{p}+\beta)^2 + V\sin(\alpha x) + Fx\right)\psi. \tag{3.4}$$

When compared to the original system, this means that the energy band structure as well as the band gaps are displaced by $\Delta p = \beta$. Apart from this shift in momentum space, the systems behavior remains otherwise unchanged.

As explained in section 2.2, we can visualize the first bandgap as a pair of barriers in momentum space. The region between these barriers corresponds to the lowest energy band of the lattice and the probability to cross the barriers equals the probability to tunnel through the first bandgap. The part of a state that does not cross the barrier stays in its adiabatic state and thus changes its momentum by an amount $\Delta p = \alpha$ corresponding to the lattice constant of the periodic potential (see figure 2.4).

Let us now consider a system that combines a static lattice as detailed in section 2.2 with this moving lattice. The Hamiltonian of such a system can be written as

$$H = -\frac{1}{2}\partial_x^2 + V_0\sin(x) + V_1\sin\big(\alpha(x-\beta t)\big) - Fx. \tag{3.5}$$

While the velocity $\beta$ did not change the behavior of the system described by equation (3.3), it plays an important role in this bichromatic lattice. Combining the moving with the static lattice results in two pairs of barriers in momentum space, one of which is shifted by $\Delta p = \beta$. Whereas shifting the position of the barriers did not introduce any new dynamics for the monochromatic lattice, the interplay between the two sets of barriers leads to interesting new effects for this

[1] This can be easily verified by following the derivation for the position of the bandgaps in section 2.2, but keeping the additional factor $\alpha$ in the phase of the lattice term.

[2] The boosted coordinate system corresponds to the transformation $\tilde{x}(t) = x + \beta t$ and $\tilde{\psi} = \psi\exp(-i\beta^2 t/2)$.

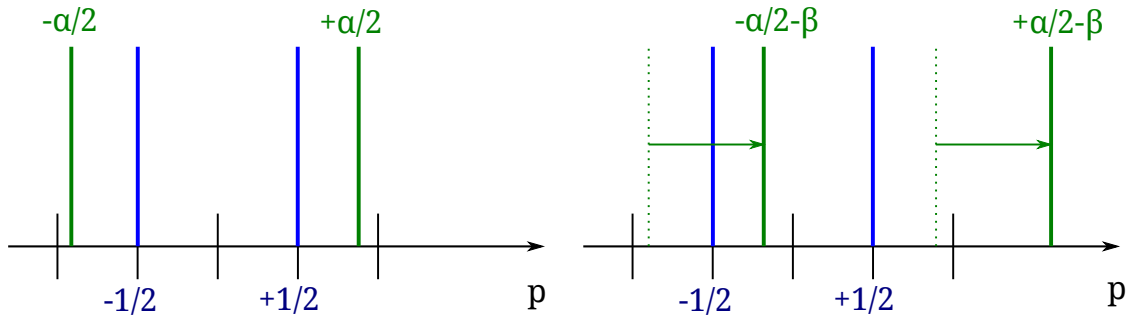


(a) Static case with $\beta = 0$

(b) The second lattice has velocity $\beta$

Figure 3.1: Combining a static and a moving lattice results in two pairs of barriers.

bichromatic lattice. The barriers corresponding to the static lattice include a region of unit length and are centered at $p = 0$. The set of barriers corresponding to the moving lattice encompass an interval of length $\alpha$ and are centered at $p = \beta$ (see figure 3.1). These barriers represent the Landau-Zener transitions the states go through at avoided crossings. The assumption that both sets of barriers act independently upon the states should therefore be valid if both these transitions happen independently and do not influence each other. This is true if the time between encountering the barriers is larger than the timescale of the Landau-Zener tunneling.

The quantity we are interested in is the probability $P_{escape}$ for a state to tunnel out of the ground band into a higher band. Let us look at some qualitative expectations how the presence of a second set of barriers in momentum space can influence this probability. A more quantitative analysis will be done in section 3.3 and 3.3, but just looking at figure 3.1, we can already get a good understanding of the interplay between the two lattices. Depending on the value of $\beta$, the two sets of barriers can be in three different configurations. In each of these configurations, we expect $P_{escape}$ to be influenced in a different way:

- For $\beta = 0$, both sets of barriers are centered at $p = 0$ as seen in figure 3.1a. This means that two barriers have to be overcome for a state to escape to a higher band. Compared to the monochromatic system with only the static lattice, the escape to higher momenta is therefore made more difficult. We thus expect a lowered escape probability $P_{escape}$.

- For $\frac{\alpha-1}{2} < |\beta| < \frac{\alpha+1}{2}$, the two sets of barriers are intertwined (see figure 3.1b). A state that is trapped between the two static barriers at $-\frac{1}{2}$ and $+\frac{1}{2}$ can therefore be reflected on the barrier belonging to the moving lattice at $p = -\frac{\alpha}{2} - \beta$. This reflection would then take it to a momentum $p = \frac{\alpha}{2} - \beta$ which lies outside of the ground band defined by the static set of barriers. A reflection on the moving lattice can thus catapult a state out

of the ground band of the static lattice. We therefore expect an increased escape probability.

- Once $|\beta|$ is larger than $\frac{\alpha+1}{2}$, both barriers belonging to the moving lattice are located outside of the ground band. Its influence on the survival probability should therefore disappear.

These qualitative predictions assume that only the bandgap between the first and the second band plays a role. If the strength of either the moving or the static lattice potential are too strong, higher bandgaps are no longer negligible. The n-th bandgap would then be represented by additional sets of barriers in momentum space. These would be located at $\pm n\alpha/2$ or $\pm n/2$ for the n-th bandgap of the moving or static lattice. As outlined in section 2.2, the influence of these higher bandgaps is however negligible for $V_0, V_1 \ll 1$.

In order to view the Landau Zener transitions as independent barriers in momentum space we furthermore assume that the distance between them is large enough. This is approximately fulfilled if the time between hitting two of the barriers is larger than the jump time $\tau_{\mathrm{jump}}$ defined in section 2.2 in equation (2.20). This condition is satisfied if the distance $\Delta p$ in momentum space $\Delta p$ between two barriers is larger than $F_0\tau_{\mathrm{jump}}$:

$$\tau_{\mathrm{jump}} = \frac{V}{\sqrt{2F_0}} < \frac{\Delta p}{F} \Leftrightarrow F_0 = \frac{2\Delta p}{V^2} \quad \text{for } V = V_0, V_1 \tag{3.6}$$

## 3.3 An Analytical Model for Noiseless Bichromatic Lattices

Based on the results of section 3.2, it is possible to build a simplified model to approximate the effects of bichromatic lattices on the escape probabilities from the ground band.

We consider the Hamiltonian

$$H = -\frac{1}{2}\partial_x^2 + V_0 \sin(x) + V_1 \sin\left(\alpha(x - \beta t)\right) + Fx \tag{3.7}$$

and model it using Landau-Zener approximations for the individual avoided crossings. Using the approximations explained in the previous section, the effect of the lattice potential can be understood as two sets of barriers in momentum space that trap the condensate between them.

When ignoring interference effects, the behavior of the condensate in momentum space can be approximated using a master equation. In this semi-classical approach, we only look at the probability density $\rho(p,t) = |\psi(p,t)|^2$ in momentum space, ignoring the phase of the wavefunction $\psi(p,t)$. The master equation governing the behavior of the wavefunction should have the following properties:

- In the region between or outside the barriers, the condensate is accelerated by the static force $F$. In regions without a barrier, the probability density in momentum space should therefore follow a flux-conservative equation with drift $F$:

$$\partial_t \rho(t,p) = -F\partial_p \rho(t,p). \tag{3.8}$$

- Close to the barriers that represent the avoided crossings, the tunneling and reflection probability should enter the master equation. We assume that the Landau-Zener transitions take place almost instantaneously and the barriers therefore have zero width in momentum space. For a barrier placed at momentum $\tilde{p}$, let us look at the probability density slightly "downstream" of this barrier at $\tilde{p} + \epsilon$, where $0 < \epsilon \ll 1$. The change in probability density there can either come from $\rho(t, \tilde{p} - \epsilon)$ tunneling through the barrier or from $\rho(t, \tilde{p} - \epsilon \pm \alpha)$ or $\rho(t, \tilde{p} - \epsilon \pm 1)$ being reflected at the barrier (see 2.4). In the limit $\epsilon \to 0$, the master equation at $\tilde{p}$ can be written as

$$\partial_t \rho(t, \tilde{p} + \epsilon) = -F\partial_p \rho(t, \tilde{p} - \epsilon) \cdot P - F\partial_p \rho(t, \tilde{p} - \epsilon \pm \alpha) \cdot (1 - P), \tag{3.9}$$

  where $P$ is the probability to tunnel through the barrier, while $(1 - P)$ is the probability of being reflected at the barrier. The sign in the second term of equation (3.9) depends on whether the left or right barrier in figure 2.4 is considered.

The solutions we are interested in are steady-state solutions that decay exponentially in time. This exponential decay corresponds to losing a fixed fraction of the probability density during each Bloch period. We therefore look for solutions of the form

$$\rho(t,p) = e^{\frac{-t}{\tau}}\rho_0(p). \tag{3.10}$$

In the barrier-free regions these solutions are governed by equation (3.8). Inserting $\rho$ from (3.10) results in

$$\begin{aligned} -\rho_p(p)\frac{1}{\tau} &= -F\partial_p\rho_p(p) \\ &\Leftrightarrow \partial_p\rho_p(p) = \frac{1}{F\tau} \equiv \gamma \\ &\Rightarrow \rho(t,p) = \rho_0 e^{-\gamma(Ft-p)} \end{aligned} \tag{3.11}$$

At the positions of the barriers, the probability density $\rho(t,p)$ will in general be discontinuous. We will therefore describe $\rho(t,p)$ by piecewise exponentially decaying solutions of the form (3.11) with discontinuities at the barriers.

The master equation for the bichromatic potential described in section 3.2 incorporates the following two sets of barriers:

- The barriers of the static lattice are situated at $\pm 1/2$ and tunneling through them happens with probability $P = \exp(-\pi V_0^2/F)$.
- The position of the barriers belonging to the second lattice is $\pm\alpha/2 + \beta$. Tunneling through them happens with the Landau-Zener probability $P' = \exp(-\pi V_1^2/F)$ as explained in section 2.2.

The solutions we are looking for are monotonously decaying steady state solutions that are piecewise defined as given in (3.11) with $\gamma$ constant for the whole solution[3]. Given such an exponentially decaying solution, the survival probability after one Bloch period is given by the decay rate:

$$P_{\text{survival}}(T_{\text{bloch}}) = e^{-\gamma F T_{\text{bloch}}} = e^{-\gamma}. \tag{3.12}$$

Once we find the parameter $\gamma$ for a given position of barriers, we can therefore directly calculate the survival probability.

When solving the master equation, we will distinguish the three different cases laid out in section 3.2 and visualized in figure 3.2. In each of the three cases the solution is defined on the three intervals $A = [a_0, a_0 + \Delta a]$, $B = [b_0, b_0 + \Delta b]$ and $C = [c_0, c_0 + \Delta c]$. On each of these intervals, we will write the solution in the form

$$\rho_A(t,p) = A_0 e^{\gamma(p - a_0 - Ft)}. \tag{3.13}$$

[3] As we are looking for steady-state solutions, the decay rate has to be time-independent.

For such solutions, equation (3.9) reduces to

$$\rho(t, \tilde{p} + \epsilon) = \rho(t, \tilde{p} - \epsilon)P + \rho(t, \tilde{p} + \pm\alpha)(1 - P). \tag{3.14}$$

We assume in all cases that the probability density left of $a_0$ is equal to zero.

Let us now solve the described master equation for each of the scenarios described in figure 3.2:

**Separated barriers:** Of the three different configurations shown in figure 3.2, the one with the completely separated barriers shown in (c) is the most straightforward to solve. It occurs for $\beta > (1 + \alpha)/2$ and writing down the equations for the interval A, we get

$$\begin{aligned} &\rho(t, a_0) = \rho(t, a_0 + \Delta a - \epsilon)(1 - P) \\ &\Leftrightarrow A_0 = A_0 e^{\Delta a \gamma}(1 - P) \\ &\Leftrightarrow \gamma = -\frac{\log(1 - P)}{\Delta a}. \end{aligned} \tag{3.15}$$

Since this already gives us all the information we need, we do not have to consider $\rho_B$ and $\rho_C$. Since $\Delta a$ is equal to one, the survival probability after one Bloch period is $P_{\text{survival}} = 1 - P$. This is exactly the same survival probability we would get in the absence of a second lattice and we can therefore conclude that the second barrier does not have any influence on the survival probability if $\beta > (1 + \alpha)/2$.

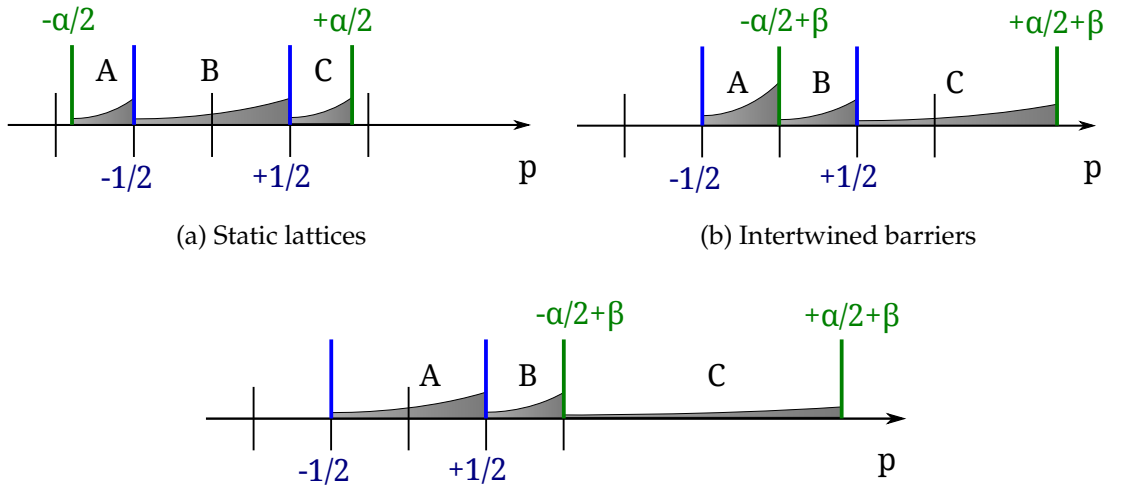


(a) Static lattices

(b) Intertwined barriers

(c) Separated barriers

Figure 3.2: The solution of the master equation depends on the relative position of the barriers corresponding to the two lattices.

**Interleaved barriers** For $\frac{\alpha-1}{2} < \beta < \frac{\alpha+1}{2}$ the two sets of barriers are interleaved (see figure 3.2b) and it is necessary to consider the full system:

$$\begin{aligned} A_0 =& B_0 e^{\gamma \Delta b}(1-P) \\ B_0 =& A_0 e^{\gamma \Delta a} P' + C_0 e^{\gamma \Delta c}(1-P') \\ C_0 =& B_0 e^{\gamma \Delta b} P. \end{aligned} \tag{3.16}$$

Inserting the first and the last equation into the second one and dividing by $B_0$ yields

$$\begin{aligned} 1 =& e^{\gamma}(1-P)P' \\ &+ e^{\gamma \alpha} P(1-P'), \end{aligned} \tag{3.17}$$

where we have already used the fact that $\Delta a + \Delta b = 1$ and $\Delta b + \Delta c = \alpha$ (see figure 3.2b). Finding a solution $\gamma$ for this transcendental equation is however only possible numerically. The decay rates will in most cases be higher than for the original Wannier-Stark problem because the second set of barriers aids in the transport of the probability density.

The case where $\frac{\alpha-1}{2} < -\beta < \frac{\alpha+1}{2}$ is also described by equation (3.17). In this case the two sets of barriers are exchanged, which leaves equation (3.17) unchanged.

**Static barriers** Lastly we treat the case seen in figure 3.2a, where the first set of barriers is located between the second set. Writing down the conditions for a solution leads to

$$\begin{aligned} A_0 =& C_0 e^{\gamma \Delta c}(1-P') \\ B_0 =& A_0 e^{\gamma \Delta a} P + B_0 e^{\gamma \Delta b}(1-P) \\ C_0 =& B_0 e^{\gamma \Delta b} P + A_0 e^{\gamma \Delta a}(1-P). \end{aligned} \tag{3.18}$$

Reduced to a single equation and using $\Delta a + \Delta b + \Delta c = \alpha$ and $\Delta b = 1$ yields

$$\begin{aligned} 1 =& -e^{\gamma \alpha}(1-P')(1-2P) \\ &+ e^{\gamma(\alpha-1)}(1-P')(1-P) \\ &+ e^{\gamma}(1-P). \end{aligned} \tag{3.19}$$

As equation (3.17), this equation can only be solved through numerical methods. Nevertheless the resulting decay rates will for all parameters be lower than the one in the original Wannier-Stark problem because the second set of barriers always impedes the escape from the ground band.

In this chapter we have built a model for the dynamics of a tilted bichromatic lattice using the Landau-Zener approximation for individual avoided crossings and ignoring all but the first bandgap. By solving the equations (3.19) and (3.17) we can make predictions for the decay rate of the ground band in this tilted bichromatic lattice. In the next section we will compare these predictions to the results of numerical simulations.

## 3.4 Numerical Simulations for the Noiseless Bichromatic Lattice

Solving the equations given in section 3.3 can give us an estimate for the decay of the survival probability in the ground band. As the model makes many assumptions that are not necessarily fulfilled, it will be interesting to see how well it matches data generated by numerical simulations of the full system. These simulations will be run using the algorithm and parameters described in chapter 4.2 and the quantity we compare is the decay rate of the survival probability in the ground band.

In figure 3.3, two curves for the survival probability in the ground band vs. time are shown for different relative velocities $\beta$ (as defined in equation (3.2)). As the state is initially prepared with a narrow momentum distribution, we expect it to go through a transition period first before settling into a steady-state solution. This is clearly visible for the curve with $\beta = 1.0$, which only decays exponentially after $t \approx 5T_{bloch}$.

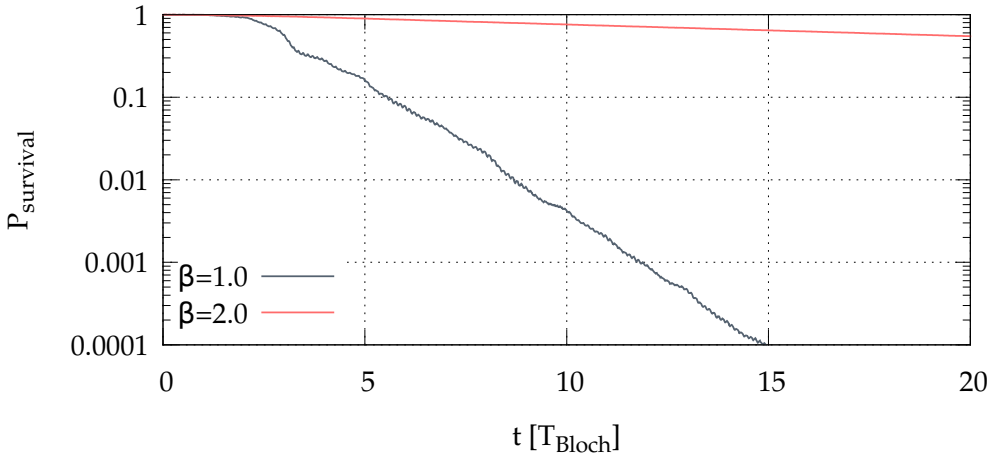


Figure 3.3: The survival probability goes through a transition period for short times but decays exponentially afterward.

Another quantity we can look at is the survival probability $P_{surv}$ at a certain time $t_0$. This time can be chosen somewhat arbitrarily but should be neither to large nor to small. Choosing $t_0$ too large leads to numerical inaccuracies as the absolute value of $P_{surv}$ becomes very small and is thus susceptible to the influence of artifacts of the numerical simulation. On the other hand, choosing $t_0$ too small will lead to inaccuracies due to a large influence of the initial state of the system (see figure 3.3). The way we measure the survival probability in the ground band is also prone to skew this quantity for small values of $t_0$.

From the model devised in 3.3, we predict that, depending on the relative velocity $\beta$, the behavior of the system can be classified into one of three cases. In

figure 3.4, numerical data for the decay rate as a function of $\beta$ is shown. The predicted borders between different cases are shown as vertical black lines. As seen in figure 3.4a, the position of these lines does indeed coincide with a drastic change in the decay rate $\gamma$. Even though the decay rates change for different values of the static force $F$, the three distinct domains remain distinguishable (figure 3.4b). This shows that qualitatively the model does correctly describe the influence of the relative velocity $\beta$ on the decay in a tilted bichromatic lattice.

A closer look at figure 3.4a reveals some interesting features. Especially in the regime where the second lattice facilitates the transport, a pattern of many local maxima and minima is visible. This pattern is most likely caused by interference effects similar to resonantly enhanced tunneling (RET) explained at the end of section 2.2.

Another interesting observation is that the figure is almost, but not completely symmetric. The slight asymmetry is caused by the fact that the static force defines a preferred direction in momentum space. For $\beta < 0$, the second lattice can only transport the wavefunction "upstream" in momentum space, from where it might again become trapped in the ground band.

For a more quantitative analysis of the model presented in section 3.3, we compare the predictions to the numerical data for a varying static force $F$. We plot the decay probability after one Bloch period calculated as $P_{surv} = 1 - \exp(-\gamma)$ vs. the inverse of the static force. This plot is often used in the literature because it allows a very straightforward comparison of the data to the Landau-Zener prediction, which shows as a straight line in the log-linear plot. We chose three fixed values for $\beta$, one out of each visible domain in figure 3.4b. The result is shown in figure 3.5. For $\beta > (\alpha+1)/2$, the model predicts a decay probability identical to the original Wannier-Stark problem given by equation (2.7). To show how well this prediction matches, the decay probability for the Wannier-Stark problem is plotted in figure 3.5b as well (labeled "monochromatic").

The local extrema observable for all values of $\beta$ cannot be accounted for in the model and makes the comparison more difficult. They can be linked to the variations in decay rate observed due to resonantly enhanced tunneling in the Wannier-Stark problem [35] mentioned in section 2.2.

As the Landau-Zener approximation constitutes the basis of our model, it does necessarily inherit all problems of this approach. This can be easily seen in figure 3.5a. The model predicts that for large $\beta$, the influence of the second lattice will vanish and the system will behave just as the Wannier-Stark system. As shown in the figure, this prediction is correct. However the predictions made by the Landau-Zener approximations cannot account for the interference effects in either the bichromatic or the Wannier-Stark-system. The predicted decay probabilities are therefore not very accurate even though they give a baseline around which the real data fluctuates.

The same problem can be witnessed in figure 3.5a, where the survival probabilities for $\beta = 0$ are compared. The prediction is again only accurate up to an order of magnitude but nevertheless describes a good log-linear fit for the data.

As predicted, the decay probability for intertwined barriers is strongly enhanced when compared to both other cases. In figure 3.5c it can however be seen that the model fails to describe the decay probabilities for small values of F. While the magnitude of the relative error is comparable to both other cases, the model consistently overestimates the decay probability in this case. Unlike the fluctuations observed in all three plots, this overestimation of the survival probabilities in figure (c) is most likely not caused by interference effects for which one would also expect enhanced decay probabilities for certain values of $1/F$.

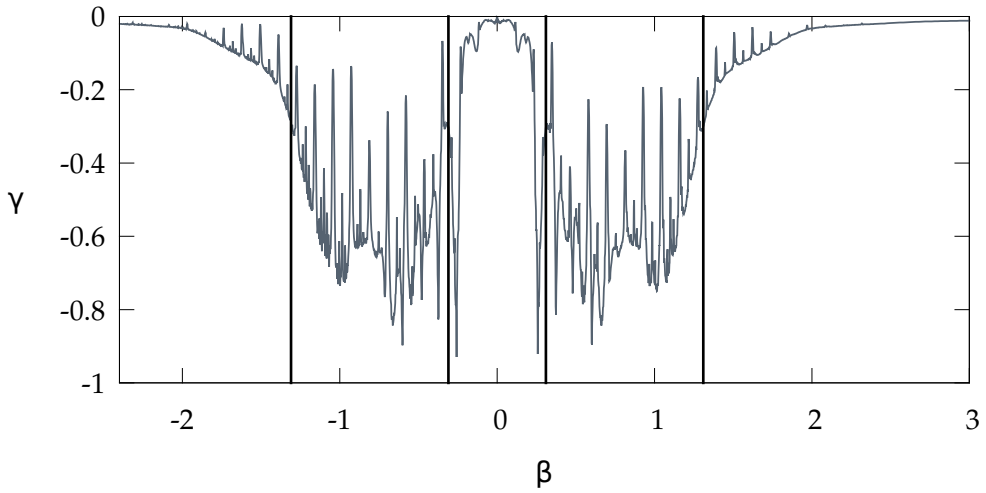


(a) The decay rate $\gamma$ for $F = \frac{1.5}{16\pi}$.

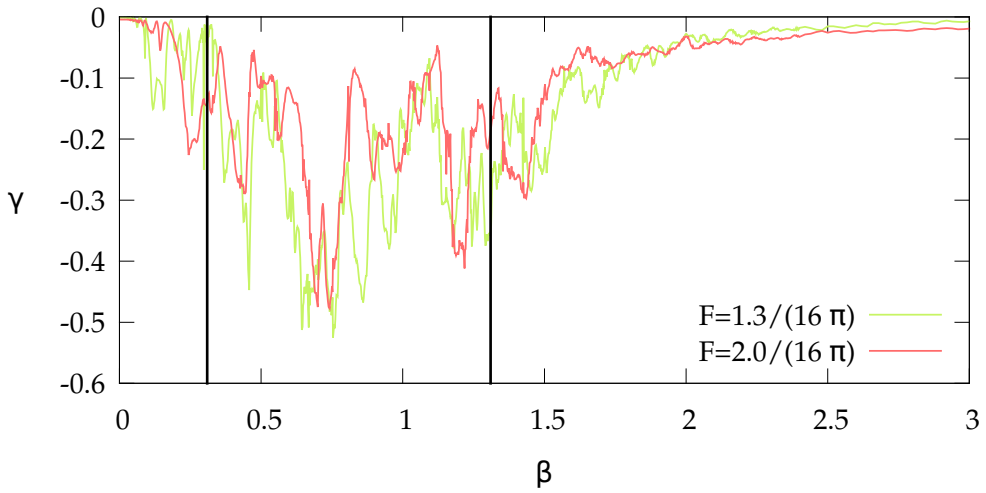


(b) The overall shape of the decay rate does not change for different F.

Figure 3.4: The decay rate $\gamma$ if the survival probability in the ground band shows a significant minimum for $\frac{\alpha-1}{2} < \beta < \frac{\alpha+1}{2}$ (marked as black lines). The parameters used for this simulation were: $V_0 = \frac{5}{16}$, $V_1 = \frac{V_0}{2}$ and $\alpha = 1.62$.

In the noise-driven system studied by Tayebirad et al. and described in chapter 2.4, the second lattice does not move with a constant velocity $\beta$. Instead $\beta$ can be viewed as a rapidly fluctuating variable. In order to understand how robust the effects observed in this section are for a non-constant $\beta$, we generate numerical data where $\beta(t)$ varies as a function of time. We will use a protocol where $\beta(t)$ is a square wave of frequency $\omega$:

$$\beta(t) = \beta_0 \cdot \mathrm{Sign}\big(\sin(\omega t)\big). \tag{3.20}$$

The analysis in this case is made more difficult by the fact that the decay of the survival probability in the ground band is not of the straightforward exponential form we see in figure 3.3. Instead there seem to be effects at many different timescales that play a role. As a very robust observable we will therefore choose the survival probability at $t_0 = 6T_{\mathrm{bloch}}$. In figure 3.6 it is clearly visible that the ef-

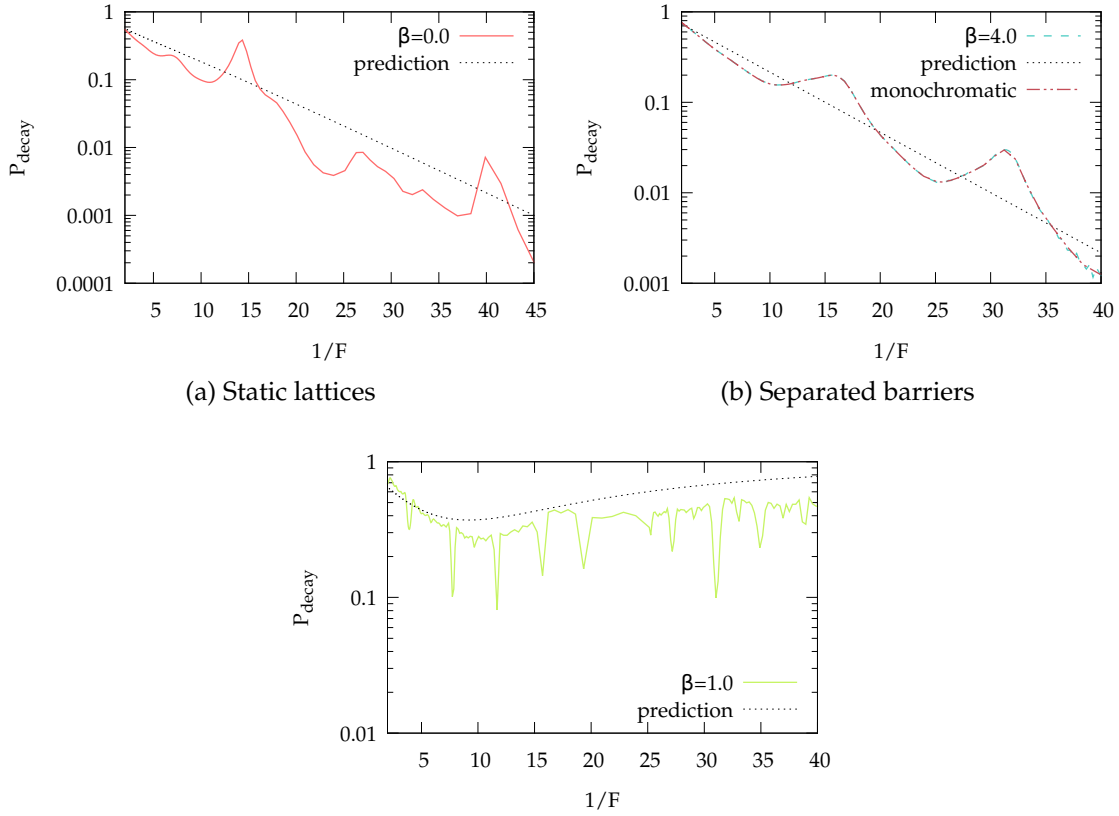


(a) Static lattices

(b) Separated barriers

(c) Intertwined barriers

Figure 3.5: Comparing the predicted decay probability $P_{\mathrm{decay}} = \exp(\gamma)$ to the value from numerical calculations shows good agreement between model and simulations. In figure (b) the decay rate in absence of a second lattice is also shown ("monochromatic"). The parameters of the system are $V_0 = 5/16$ and $V_1 = V_0/2$.

fect of this alternating β cannot be neglected. For high frequencies $\omega > 13\omega_{\text{bloch}}$ the influence of the second lattice vanishes. For lower frequencies however it changes the picture considerable. Especially for large values of β where the two sets of barriers are completely separated, this alternating β enhances the decay rate to the point where it becomes indistinguishable from the system with interleaved barriers.

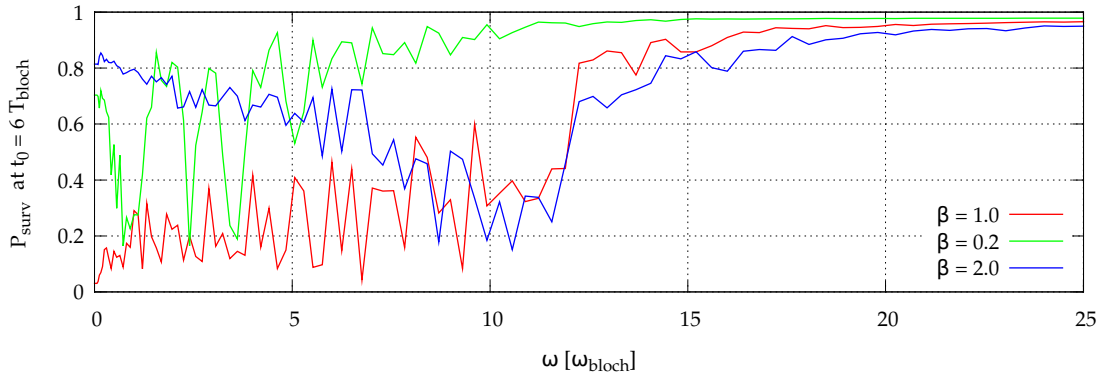


Figure 3.6: A non-static β alternating with frequency ω changes the survival probabilities in the ground band. The values of β have been chosen to represent the three domains distinguished by the model. The parameters of the system are $V_0 = 5/16$, $V_1 = V_0/2$ and $F = 1.5$.

For a fluctuating value of β which could for example be the result of a noise-driven lattice, we therefore expect an enhanced decay rate for large values of β.

# 4 Numerical Studies of Bose-Einstein Condensates in Noise-driven Bichromatic Lattices

## 4.1 A Simple Model for Noise-driven Bichromatic Lattices

The model presented in chapter 3 has proven effective in describing the noise-free bichromatic lattice. This analysis of the noise-free system will help us to better understand the properties of the noise-driven system.

The full noise-driven system is described by the Hamiltonian

$$H = -\frac{1}{2}\partial_x + V_0 \sin(x) + V_1 \sin\big(\alpha(x - \phi(t))\big) - Fx, \tag{4.1}$$

where $\phi(t)$ has its usual meaning as a harmonic noise process. As a first estimate of the influence of the noise on the system we can approximate the harmonic noise process as being linear in time through a first-order expansion:

$$\phi(t) \approx \phi_0 + \dot{\phi} t \tag{4.2}$$

with $\phi_0$ and $\dot{\phi} = \beta$ constant. In this case the Hamiltonian in equation (4.1) reduces to the Hamiltonian of the noise-free bichromatic system introduced in chapter 3.

Considering the stochastic differential equation of the harmonic noise (see section 2.3):

$$\begin{aligned} \dot{\phi} &= \nu \\ \dot{\nu} &= -2\Gamma\nu - \omega_0^2\phi + \sqrt{4T\Gamma}\,\xi(t), \end{aligned}$$

the approximation $\dot{\phi} = \nu = \text{const}$ corresponds to the limit $\Gamma, \omega_0 \to 0$.

In section 2.3 we found that the noise variable $\nu$ follows a Gaussian distribution with variance $T$. In the limit $\Gamma, \omega_0 \to 0$, the variable $\nu$ can hence be treated as a constant following the Gaussian distribution

$$P(\nu = \beta) = \frac{1}{\sqrt{2\pi T}} \exp\left(\frac{\beta^2}{2T}\right). \tag{4.3}$$

From chapter 3 we know how interband tunneling in the bichromatic lattice system is influenced by the velocity $\beta$ of the second lattice. Assuming that $\beta = \nu$

follows the distribution (4.3), the expectation value of the survival probability $\langle P_{surv}(t_0)\rangle$ at a time $t_0$ is given by

$$\langle P_{surv}(t_0)\rangle = \int_{-\infty}^{+\infty} P(\nu = \beta) P_{surv}(t_0, \beta) d\beta, \tag{4.4}$$

with $P_{surv}(t_0, \beta)$ given either by the numerical or predicted values given in chapter 3.4. In the same vein the expected decay rate $\langle\gamma\rangle$ can be calculated as

$$\langle\gamma\rangle = \int_{-\infty}^{+\infty} P(\nu = \beta)\gamma(\beta) d\beta. \tag{4.5}$$

The result of this integral for different values of $\langle\nu^2\rangle = T$ is plotted in figure 4.1. It can be seen that $\langle\gamma\rangle$ has a clear maximum for intermediate values of T. Going back to figure 3.4b we can see the reason for this:

- For small values of T, the Gaussian distribution $P(\nu = \beta)$ is very narrow and only the peak of $\gamma(\beta)$ around zero contributes to the integral (4.5). The expectation value $\langle\gamma\rangle$ should therefore be equal to the value $\gamma(0)$ at the origin. This corresponds to a static lattice (as shown in figure 3.2a).

- Once T is large enough such that the distribution also covers values of $\beta$ that lie within the minimum between $(\alpha-1)/2 < \beta < (\alpha+1)/2$, the value of $\langle\gamma\rangle$ starts to decline. This corresponds to a lattice moving fast enough such that at some times the barriers in momentum space are found in an interleaved configuration (see figure 3.2b).

- When further increasing T, the distribution reaches a point where it is broad enough that contributions from $\beta > (\alpha+1)/2$ start to play a role. In this regime, which corresponds to completely separated pairs of barriers, the decay rate is similar again to the one at $\beta = 0$. The value of $\langle\gamma\rangle$ thus declines once the contributions from this regime become dominant.

As shown in section 3.4, the values for $P_{decay}(\beta)$ and $\gamma(\beta)$ predicted by the model for bichromatic lattices are only accurate to a factor of $\sim 2$ for the parameters chosen here. The predicted decay rates therefore differ by a similar factor. It should however be noted that the overall shape of the curve remains the same. This is due to the fact that while the model does not produce accurate values for $\gamma(\beta)$, it does correctly predict the existence and boundaries of the three regimes. For all future comparisons we will nevertheless use the curve calculated with the numerical data for $\gamma(\beta)$ since it describes the actual effect of a moving lattice on the system more accurately.

Overall the model predicts that the noise-driven lattice averages over the effects already observed for the bichromatic lattice with a constant relative velocity $\beta$ in chapter 3. The effects occurring in this constantly moving lattice correspond to the three regimes illustrated in figure 3.2. All that the harmonic noise process

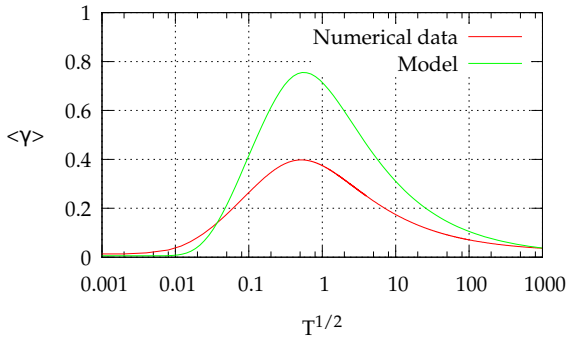


Figure 4.1: Predicted decay rate for $V_0 = \frac{5}{16}$, $V_1 = \frac{V_0}{2}$ and $F = \frac{1.5}{16\pi}$ using either the model discussed in section 3.3 or the numerical data presented in 3.4.

does in this picture is adding up the contributions of these three different effects with a relative weight that depends on the noise parameter $T$.

This simplified model ignores most of the properties of the underlying noise process and is only exact for $\omega, \tau = 0$. It will therefore not be able to describe the data from the noise-driven tilted lattice system exactly. In the next paragraphs we will therefore discuss what additional effects should occur in the full system and how they can affect the tunneling rate.

To understand these effects it is again instructive to imagine the effect of the noise lattice as a pair of barriers in momentum space. The model assumes that the initial position of these barriers is randomly distributed but does not change with time. However, when the lattice is driven by a real noise process, the position of these barriers is not static. They instead move in momentum space with a velocity $\dot{\nu}$ corresponding to the acceleration of the lattice. In the case $\Gamma = 0$, the barriers perform sinusoidal oscillations in momentum space. Furthermore for $\Gamma \neq 0$ the position of this barriers in momentum space is not even continuous in time since $\nu$ is governed by the diffusion-like equation

$$\dot{\nu} = -\Gamma\nu - \omega_0^2\phi + \sqrt{4\Gamma T}\xi(t) \tag{4.6}$$

with a white noise term $\xi(t)$ (see section 2.3).

The non-static position of these barriers in momentum space will of course have an influence on their effect on the system. The probability to tunnel through a barrier is approximately given by the Landau-Zener probability given in section 2.2

$$P_{LZ} = \exp\left(-\pi\frac{V_0^2}{|f|}\right), \tag{4.7}$$

where $f$ denotes the sweeping rate with which the states go through the transition. In the case of an accelerating lattice, this rate $|f|$ corresponds to the relative speed between the state and the barrier. The state is driven by the static force $F$

and while the barrier is driven by the noise process. In this case the relative speed is $|f| = |F - \dot{\nu}|$, which depending on the value of $\dot{\nu}$ can be larger or smaller than $|F|$.

It should be mentioned that, strictly speaking, $\dot{\nu}$ is not a well-defined quantity because the noise term in equation (4.6) has infinite variance. For finite times $h$ the value of $\dot{\nu}$ can however be approximated using finite differences of $\nu$. Looking at the variance of this finite time difference

$$\begin{aligned}\left\langle \left( \frac{\nu(t+h) - \nu(t)}{h} \right)^2 \right\rangle \approx & \Gamma^2 \langle \nu^2 \rangle + \omega_0^4 \langle \phi^2 \rangle \qquad (4.8)\\ & + \frac{\sqrt{4T\Gamma}}{h^2} \left\langle \int_t^{t+h} \int_t^{t+h} \xi(t')\xi(t'')dt'dt'' \right\rangle \\ = & \Gamma^2 T + \omega_0^2 T + \frac{\sqrt{4T\Gamma}}{h}, \qquad (4.9)\end{aligned}$$

we can see that for finite timescales $h$ the term has a standard deviation of at least

$$\sqrt{\mathrm{Var}(\dot{\nu})} \geqslant \sqrt{T(\omega_0^2 + \Gamma^2)}. \qquad (4.10)$$

If this value is larger than $F$, the relative sweeping rate $|f| = |F - \dot{\nu}|$ will in average be increased and tunneling through the corresponding barrier is therefore strongly enhanced.

Additionally the noise term in equation (4.6) will also have an influence on Landau-Zener transitions. Analysis of this problem shows that this noise term would influence the diagonal terms of the Landau Zener Hamiltonian (2.17). As known from the work of Kayanuma et al. [19, 20], strong diagonal noise in Landau-Zener transitions leads to a mixing between both states. Independently of its initial state, the system ends up in either of the states with equal probability after the transition. This effect is more pronounced when the coupling between both states is strong.

For fast noise with large $\Gamma$ or $\omega_0$, we therefore expect that the probability of reflection on the second lattice is strongly suppressed. In this regime, the influence of the noise lattice should therefore vanish faster than predicted by the model.

## 4.2 Algorithm and Implementation

### The observable

In the last chapter, the main observable of the system was the decay rate $\gamma$ of the survival probability in the ground band. This observable was calculated by fitting the survival probability $P_{surv}(t)$ with an exponential function. The underlying assumption behind this was that after a short transition period, $P_{surv}(t)$ undergoes an exponential decay at a constant rate $\gamma$.

If $P_{surv}(t)$ is however influenced by a stochastic variable $\phi(t)$ that changes over time, there is no inherent reason for this decay to stay constant. In section 3.4 we have already seen that exponential decay is only visible after the system had enough time to settle into a steady-state. Under the influence of a stochastic process, it is not guaranteed that the system ever reaches such a steady state. The decay rate $\gamma(t_0, \phi(t))$ of the survival probability should hence not only depend on the noise realization $\phi(t)$, but also on the time $t_0$. As a consequence, observing the decay rate $\gamma(t)$ is not as straightforward as it has been for the numerical simulations presented in chapter 3.4, since we cannot simply fit the decaying survival probability for one noise realization with an exponential function.

The quantity we are actually interested in is the expectation value of the decay rate $\langle\gamma\rangle_{noise}$ averaged over the noise realizations. While $\gamma$ does not necessarily assume a constant value for a single noise realization $\phi(t)$, we can assume that the average decay rate $\langle\gamma\rangle_{noise}$ reaches an equilibrium value due to the ergodic property of the noise process.

Let us look at the way the survival probability in the ground band is influenced by a non-constant decay rate $\gamma$ [44]:

$$\dot{P}_{surv}(t_0) = -\gamma(t_0)P_{surv}(t_0) \tag{4.11}$$

$$\Rightarrow P_{surv}(t_0) = \exp\left(-\int_0^{t_0}\gamma(t')dt'\right). \tag{4.12}$$

Averaging the logarithm of the survival probability over noise realizations thus results in

$$\left\langle \log\left(P_{surv}(t_0)\right)\right\rangle_{noise} = -\int_0^{t_0}\langle\gamma(t')\rangle_{noise}dt'. \tag{4.13}$$

Assuming that $\langle\gamma(t_0)\rangle_{noise}$ remains constant after an initial equilibration time $t_{equ}$, this quantity should fall off linearly:

$$\left\langle \log\left(P_{surv}(t_0)\right)\right\rangle_{noise} = -\int_0^{t_{equ}}\langle\gamma(t')\rangle dt' - \langle\gamma_{equ}\rangle(t - t_{equ}). \tag{4.14}$$

The value of $\langle\gamma_{equ}\rangle$ can thus be estimated by fitting a linear function to $\langle\log P_{surv}(t)\rangle$. For this it is necessary to average $P_{surv}(t)$ over multiple noise process realizations.

## Numerical Simulations

The data presented in this work has been generated using numerical simulations of the one-dimensional Schrödinger equation and the three-dimensional Grosz-Pitaevskii equation. For the one-dimensional system, the following protocol was employed to perform the simulations:

- A random phase $\phi_0 \in [0 : 2\pi[$ was chosen and a harmonic noise initialized in a random state $\phi(0)$ according to its equilibrium distribution (see section 2.3). The initial Hamiltonian was set to

$$H = -\frac{1}{2}\partial_x^2 + V_0 \sin(x) + V_1 \sin\left(\alpha(x - \phi_0 - \phi(0))\right) + \tilde{\omega}^2 x^2, \tag{4.15}$$

  where $\tilde{\omega}$ is the frequency of the harmonic trap.

- Using this initial Hamiltonian, the imaginary time algorithm presented in appendix B was used to equilibrate the system. To this end the time step $\Delta t$ was decreased repeatedly to make sure the system had converged to the ground state.

- The harmonic trap was disabled and instead the static force $F$ was applied resulting in the new Hamiltonian

$$H = -\frac{1}{2}\partial_x^2 + V_0 \sin(x) + V_1 \sin\left(\alpha(x - \phi_0 - \phi(t))\right) - Fx, \tag{4.16}$$

  where the time-dependent phase $\phi(t)$ is defined by the harmonic noise process.

- Governed by this time-dependent Hamiltonian, the system is evolved using the Crank-Nicolson algorithm described in appendix B.

- In regular intervals we measure the survival probability in the ground band. In order to obtain the wavefunction in momentum space for the numerical data, a Fourier transform along the $x$-axis is applied to the wavefunction by using the FFTW library [14]. How the survival probability was computed from the wavefunction in momentum space is explained in the next paragraph.

To generate the harmonic noise process, the algorithm described in appendix A was used. The needed Gaussian random numbers were generated using a Box-Muller algorithm fed by a Mersenne-Twister pseudo-random number generator, both implemented in the GNU Scientific Library [15].

The observable we are interested in is the probability to remain in the ground band of the Wannier-Stark system (2.7). Since the presence of a second lattice significantly alters or even destroys the band structure, we cannot simply project the wavefunction on the states associated with this ground band. We will instead

measure the probability to find the system in a state with a momentum $|p| < 2.5$. Equating this measure with the survival probability in the ground band of the monochromatic system makes two assumptions:

- The states belonging to the ground band of the Wannier-Stark problem are mainly located within the boundaries in momentum space. In figure , it can be seen that for $V_0 = 5/16$, the probability for a ground band state to be found outside these barriers is less than $10^{-5}$.
- Any state that tunnels from the first into the second band will be accelerated further out of these boundaries. This assertion was discussed in section 3.3 and is approximately true for systems where $V \ll 1$ (see also discussion in [28]).

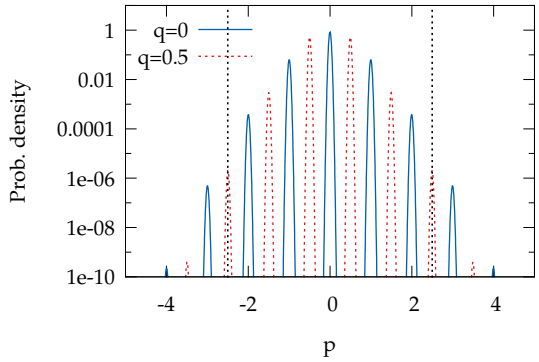


Figure 4.2: Relative momentum probability density of two ground band states for Hamiltonian (2.7) with $V = 5/16$. The lines at $q = \pm 2.5$ are the boundaries used for measuring the survival probability. The state at $q = 0$ is the ground state of the system.

This means that any part of the wavefunction that tunnels through the first band gap will eventually go through these boundaries at $\pm 2.5$, even though this does not happen immediately. If the second condition is fulfilled, any part of the wavefunction that has once left the ground band will experience a linear growth in momentum. It will therefore cross the right barrier seen in figure 4.2 after a fixed amount of time. Choosing larger values of p for the position of this barrier therefore only delays the decrease of $P_{surv}$ by a fixed amount of time, but does not slow down the exponential decay.

Due to the random nature of the noise, it is necessary to average the observable over several realizations of the stochastic process. The number of realizations needed depends on the desired accuracy. We are mostly interested in the expectation value of the decay rate and the survival probability. The expectation value of a quantity $A$ can be estimated by calculating

$$\bar{A} = \frac{1}{N} \sum_{i=0}^{N} A_i, \tag{4.17}$$

where $A_i$ is the quantity $A$ measured using the $i$-th realization of the noise process. As a sum over stochastic variables $\bar{A}$ is itself a stochastic variable with expectation value $\langle \bar{A} \rangle = \langle A \rangle$ and variance $\langle \bar{A}^2 \rangle = \langle A^2 \rangle / N$. The accuracy of this estimate thus scales as $\mathrm{StdDev}(A)/\sqrt{N}$. If not stated otherwise, the number of noise realizations used for all data in this chapter is $N = 20$. This number proofed to be sufficient to reduce the errors of the mean enough to describe the behavior of the system and to allow a comparison with the predictions made by our model [38]. In all following figures, the error bars of the data denote the statistical error of the values estimated through:

$$\mathrm{StdDev}(\bar{A}) \approx \frac{\sqrt{\sum_{i=0}^{N} (A_i - \bar{A})^2}}{N}. \tag{4.18}$$

## 4.3 Numerical Results for Harmonic Phase Noise

In this section we will analyze the results of the numerical calculations and compare them to the predictions made by the model constructed in section 4.1.

The model predicts that from the three noise parameters only $T$ has a discernible influence. We will therefore first look at the decay rate $\gamma$ as a function of this quantity while keeping $\omega_0$ and $\Gamma$ fixed. In figure 4.3, the decay rate of the system is plotted against $T$ for different values of $\omega_0$. The third noise parameter $\Gamma$ has been set to a fixed value of 5. The overall shape of all curves but one is similar and has a maximum observed around $T \approx 0.5$. The exception is the curve with the highest frequency, for which the tunneling rate for small $T$ seems to be suppressed. With the exception of this curve, the influence of $\omega_0$ is negligible, which is verified by the plot in figure 4.4a.

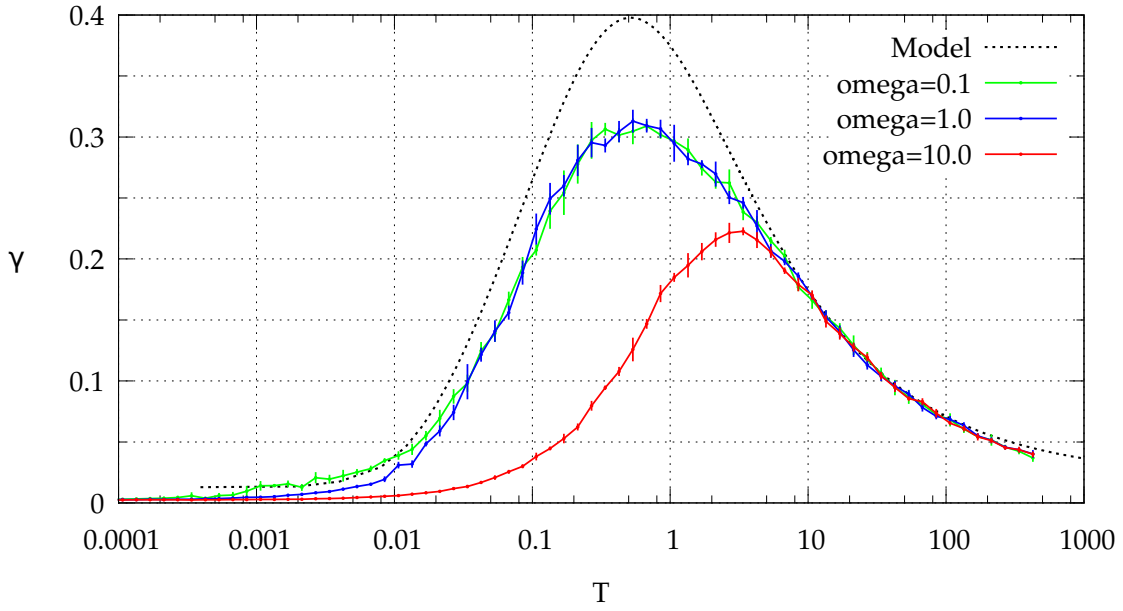


Figure 4.3: Decay rates of the bichromatic noise system with noise paramter $\Gamma = 5$. The error bars denote the statistical error caused by using only a finite number of noise realizations. The lattice parameters are $V_0 = 5/16$, $V_1 = V_0/2$, $F = 1.5/(16\pi)$ and $\alpha = 1.62\ldots$

The overall shape of the curve is described well by the model, but when comparing the predictions with the numerical data, many differences are visible. The most prominent is that even though the location of the maximum is predicted correctly, the maximal decay rate is overestimated by the model. While this difference is most eye-catching at the maximum, it follows a general trend visible for all values of $T$: the model gives a higher bound of the decay rate, but the actual values are only accurate for very large $T$. This is also visible for $T < 0.001$, where the predicted tunneling rate is about a factor of five higher than the actually ob-

served rate.

These differences become understandable in the light of the approximations made by the model. In section 4.1 when talking about the shortcomings of the model we predicted that the influence of the moving lattice would be suppressed if the noise-term was too fast. Since the model predicts that for large T the influence of the second lattice vanishes, it is no surprise that the predictions in this region describe the data very well.

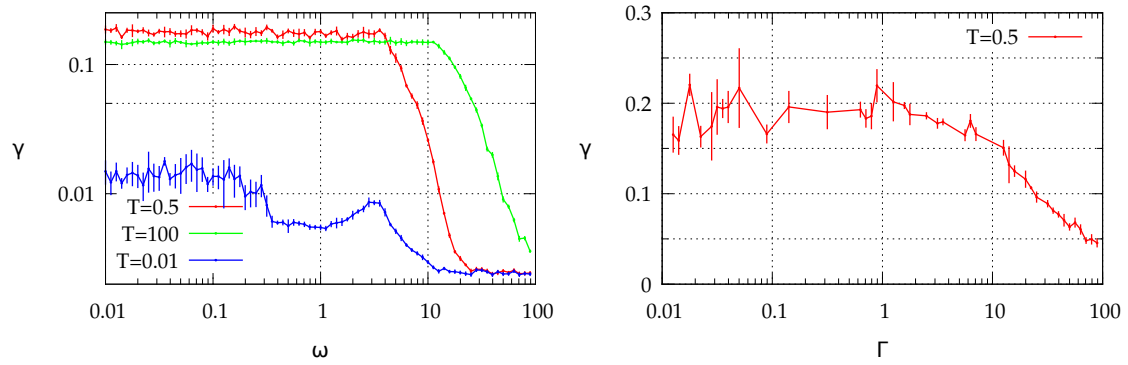


(a) Damping parameter fixed to $\Gamma = 5.0$

(b) Frequency fixed to $\omega_0 = 0.0001$

Figure 4.4: Influence of $\Gamma$ and $\omega_0$ on the decay rate for different values of T

But reducing $\omega_0$ does still not bring the data in accordance with our model. While the tunneling rates do hardly change between $\omega_0 = 1.0$ and $\omega_0 = 0.1$, both are still far from the tunneling rates predicted by the model. The reason for this lies in the third noise parameter $\Gamma$. Looking at equation (4.10) we can see that the sweep rate f through the Landau-Zener transition is also influence by this term. Especially the white noise term $\sqrt{4\Gamma T}$ scales with the square root of this parameter. As mentioned in section 4.1, this should also lead to a reduced influence of the noise-driven lattice.

While the model assumes that the second lattice is static, both the noise parameters $\omega_0$ and $\Gamma$ accelerate the second lattice and thus impede its ability to transport the state out of the ground band.

To further investigate the influence of the noise parameter $\Gamma$, we recreate the previous plot but set $\Gamma = 0$. As seen in figure 4.5 the results are similar to the ones observed for $\Gamma = 5.0$. There are however important differences that clearly show the influence of this noise parameter on the transport properties of the system.

A first observation is that the error bars of this data are much larger than the ones where $\Gamma \neq 0$. This is despite the fact that averages were taken over four times as many noise realization. The reason of these increased statistical fluctuations is that with $\Gamma$ set to zero the harmonic noise process reduces to an undamped harmonic oscillation. The noise process is initialized with an initial state according to its equilibrium distribution. The amplitudes of the harmonic oscillations for $\Gamma = 0$ are therefore initialized following a Gaussian distribution but do not change over

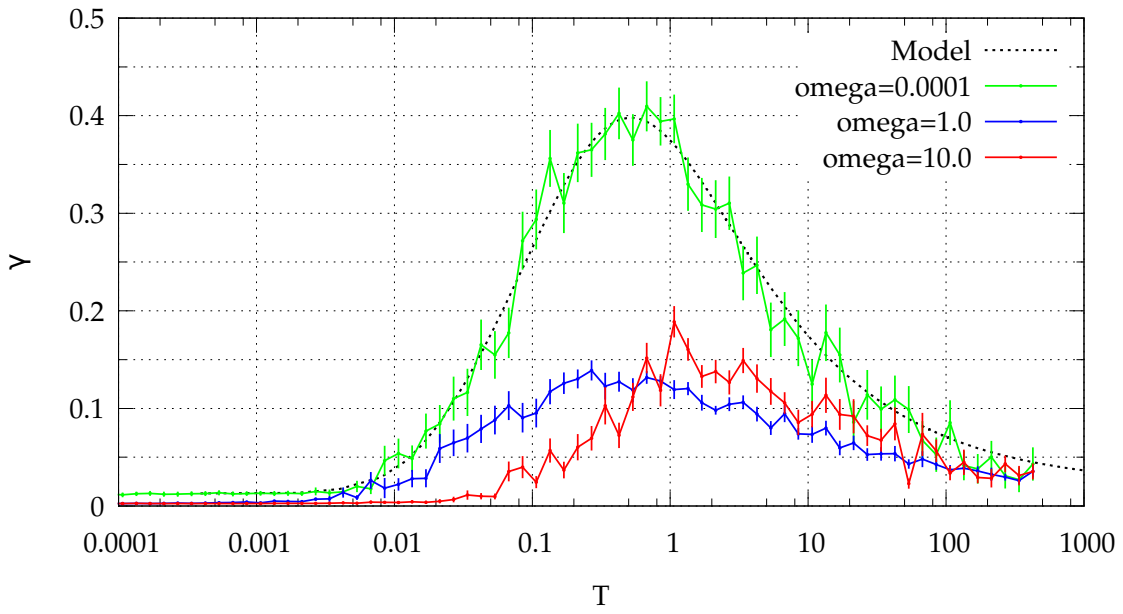


Figure 4.5: Decay rate $\gamma$ for a system with noise parameter $\Gamma = 0$. All other parameters are identical to the plot in figure 4.3.

time. While the equilibrium distribution of the noise process is independent of $\Gamma$ (see section 2.3, the ergodicity of the process is lost for $\Gamma = 0$. A strong damping constant ensures that even a single noise realization equilibrates over time, reducing the variance of noise properties if they are averaged over a time longer than $1/\Gamma$. For $\Gamma$ very low or equal to zero this equilibration does not take place anymore, leading to an increased variance of measured noise properties.

Despite the large fluctuations for the numerical data, figure 4.3 shows that for $\Gamma = 0$ and very low frequencies the model proposed in section 4.1 describes the system accurately for all values of T. Whereas this leads to increased decay rates for $\omega_0$ very small, for higher frequencies the influence of the noise lattice is actually reduced.

We also want to look at harmonic noise processes with a fixed variance $\langle \phi(t)^2 \rangle$, comparable to those used in previous work by Tayebirad et al. [38]. For these noise processes, $\omega_0$ and T are coupled through the relation

$$\omega_0 = \sqrt{\frac{T}{\langle \phi^2 \rangle}}. \tag{4.19}$$

This means that increasing T also implies an increased $\omega_0$.

In the work of Tayebirad et al., the survival probability at a fixed time $t_0$ was observed as a function of a rescaled noise frequency

$$\begin{aligned} \omega' &= \omega_0 \cdot \sqrt{\langle \phi^2 \rangle} \\ &= \sqrt{T}. \end{aligned} \tag{4.20}$$

The quantity $\omega'$ only depends on the noise temperature T and the survival probability at a time $t_0$ is approximately given by $\exp(-\gamma t_0)$ [1]. We can therefore continue using plots of $\gamma(T)$ and still compare our results to the ones found by Tayebirad et al.

The resulting decay rates are shown in figure 4.6. From the previous observations we know that the model only describes the data well for slow noise processes.

Focusing on the comparison between the model and the data, it can be seen that the difference between model and observed data grows for noise processes with small variances. Due to relation (4.19) this corresponds to fast noise processes.

For the noise process with $\langle\phi^2\rangle = 0.1$, the frequency of the noise grows so rapidly that the shape of the curve is changed. While the model describes the system accurately for low values of T, at $T \approx 0.1$ the fast noise term starts to suppress the effect of the second lattice. This counteracts the increase in decay rate we would otherwise observe around this value of T. Even for the noise process with unit variance we observe a disagreement between data and model at $T \approx 10$.

Using the model we can therefore explain the behavior of such systems with a fixed variance noise process. Comparing with figure 4.3, the universal scaling

[1] This relation is only approximately true as a system prepared in a non-equilibrium state will first go through a transition period before reaching a decaying steady state. For small values of $t_0$ the decay can therefore not be described by a single exponential function.

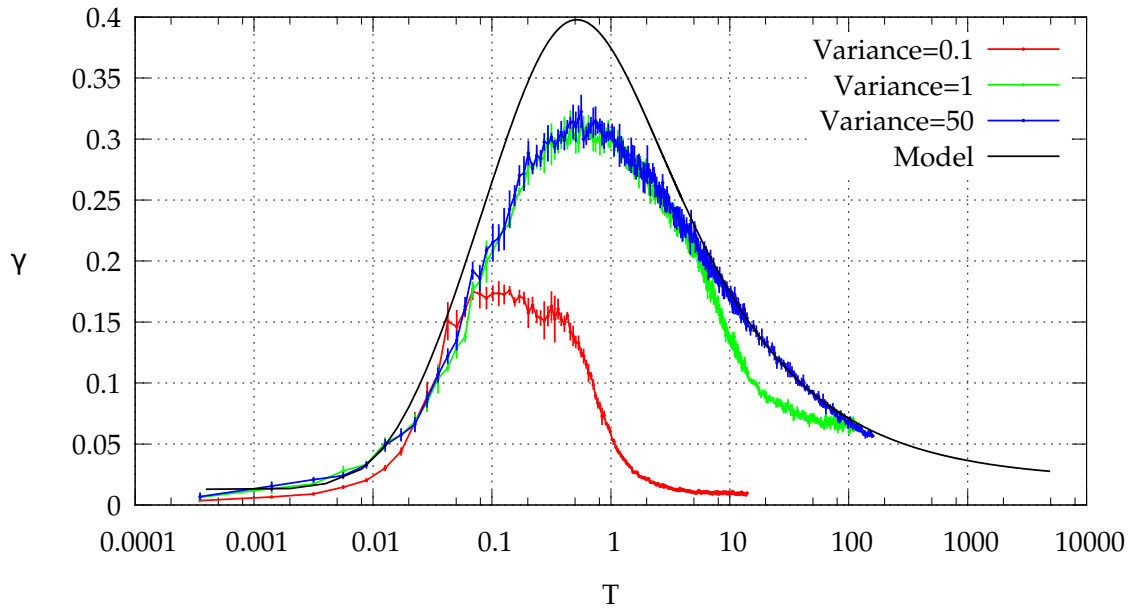


Figure 4.6: The decay rate $-\gamma$ for different noise processes with fixed variance $\langle\phi^2\rangle$. The parameters of the system are: $V_0 = \frac{5}{16}$, $V_1 = \frac{V_0}{2}$, $F = \frac{1.5}{16\pi}$ and $\Gamma_{noise} = \frac{5}{T_{Bloch}}$

observed by Tayebirad et al. can be seen to be the limiting behavior for $\omega_0 \to 0$. In this limit the decay rate $\gamma(T)$ does not depend on $\omega_0$ but only on the damping constant $\Gamma$ and the noise temperature T.

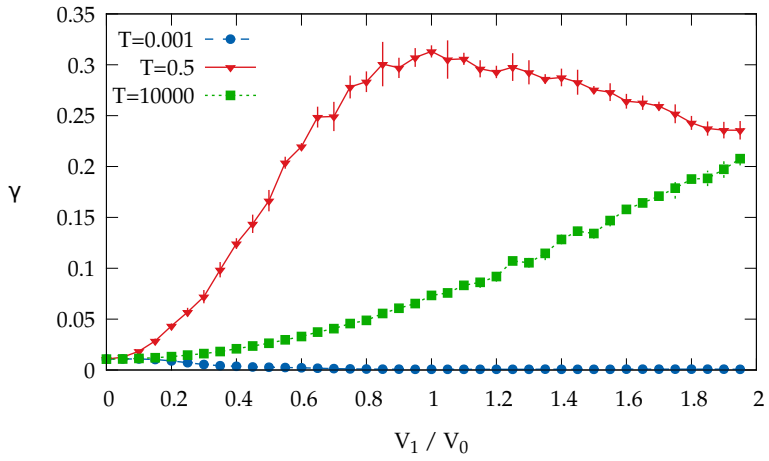


Figure 4.7: Decay rate $\gamma$ for different noise lattice amplitudes. The system parameters are $F = \frac{1.5}{16\pi}$, $V_0 = \frac{5}{16}$ and the noise process uses the parameters $\omega_0 = 1.0$ and $\Gamma = 5.0$.

The calculations by Tayebirad et al. were performed with a noise lattice of the same amplitude as the static lattice: $V_1 = V_0$. In contrast, the data presented in this section was created with a weaker noise lattice: $V_1 = 0.5V_0$. In order to make sure that the observed effects do not depend on the ratio between $V_1$ and $V_0$, we observe the system for different values $V_1$ while keeping $V_0$ fixed. We choose fixed noise temperatures T representative of the three different regimes observed in the previous plots. The result of this calculations can be seen in figure 4.7. We would expect that an increased amplitude of the noise lattice would enhance effects visible in the system. Increasing $V_1$ would therefore suppress tunneling for low values of T, enhance it for $T \approx 0.5$ and leave the tunneling rates for very large T almost unchanged. Looking at the plot we can however see that these estimates are only correct for small values of $V_1$, while tunneling rates for $V_1 > V_0$ cannot be adequately explained through our model. It can be argued that for a strong second lattice with large $V_1$, the system is effectively trapped by this second potential and the influence of the first potential with the comparatively small strength $V_0$ becomes negligible. In the model introduced in section 3.2 and 3.3, this would mean that the state is trapped between two barriers that are themselves moving in momentum space. It is clear that in this case the measurement of the survival probability as shown in figure 4.2 can not accurately reflect the dynamics of the system anymore.

# 5 Conclusion and Outlook

## 5.1 Conclusion

In this diploma thesis we studied the interband transport properties of tilted bichromatic optical lattices. Although we mainly focused on the case where one of the lattices is driven by a noise process, we also found interesting results for the case where one lattice is moving with a constant velocity.

In chapter 3 we analyzed the characteristics of a system where the second lattice is moving with a constant velocity $\beta$ relatively to the first one. Within the investigated parameter range we found that the transport properties of this system are strongly influenced by this relative velocity $\beta$. If both lattices are at rest, the second lattice suppresses the transport of the wavefunction because it represents an additional barrier that must be overcome in order to escape from the ground band. If the second lattice is moving very quickly, its effect on the system disappears since the rapidly fluctuating potential averages out to zero. Between these two limiting cases there is however a range of velocities where the interband transport is assisted through reflections on the moving lattice.

A model that predicts the relative velocity $\beta$ where this transition between assistance and suppression of the tunneling process occurs was introduced and compared to the results of numerical investigations. For the parameter range covered in the numerical calculations, the model was able to qualitatively predict the transition velocities.

Since even small changes in the relative velocity $\beta$ lead to large jumps in the interband tunneling rate (see figure 3.4), these kind of bichromatic systems could be used for experiments where it is necessary to coherently control Bose-Einstein condensates in optical lattices.

In chapter 4, we studied a system where the second lattice was driven by a harmonic noise process. Using the results from chapter 3, we were able to formulate a model for the influence of slow harmonic noise. According to this model, only the noise temperature T has a significant influence on intraband tunneling. The model predicts driving the second lattice through a noise-process leads to an averaging between assisted and suppressed tunneling. The relative contribution of those two effects is determined by the noise temperature T. For low values of T, the suppressive effect is dominant, while the contribution of assisted tunneling is maximized if $T \approx 1$ in the units used in this work. We compared these predictions to the results of numerical simulations and found that, for the range of parameters covered by the simulations, the model correctly described the system in the presence of slow harmonic noise. Leaving this slow noise regime and increasing the

noise parameters $\Gamma$ or $\omega_0$ lead to a suppressed influence of the noise-driven lattice for all investigated parameters. However even out of the slow noise regime, intraband tunneling was maximized for $T \approx 1$.

Earlier work by Tayebirad et al. on the same system found indications for a universal scaling behavior. Within the framework of the model presented in section 3.3, this behavior can be understood as an effect of reaching the slow noise limit.

When comparing the effects of the noise-driven bichromatic lattice to the one with a constant relative velocity, we were not able to find any new effects that were caused by the temporal disorder. Instead we found that the noise process leads to an averaging over the effects already found in the bichromatic system with a constant relative velocity.

## 5.2 Open Questions

The model we presented for bichromatic lattices with a constant relative velocity correctly predicts the transition between assisted and suppressed transport, but the predictions of the actual decay rates are quantitatively not very accurate. The reasons for the large gap between simulated data and the predictions made by the model are most likely due to interference effects which do not enter the model. It is known that these interference effects have a large influence on interband tunneling in the Wannier-Stark problem, where this influence is called resonantly enhanced tunneling. We therefore expect a similar influence for the bichromatic Wannier-Stark problem.

In order to include these interference effects into the model, it would be necessary to know the exact energies of all involved states. Once these are known, a complex amplitude version of the constant flux master-equation from section 3.3 could be formulated and solved. The solutions of this equation would take interference effects into account and should therefore be able to describe the bichromatic noiseless system much more accurately.

In the form presented in this work, the model for the effect of harmonic noise on bichromatic lattices can only account for the influence of one of the three noise parameters. While this parameter $T$ was found to have a much stronger influence on interband tunneling than the other parameters, their influence can nevertheless not be completely neglected. In section 4.1 we gave some estimates about the influence of the two remaining parameters $\Gamma$ and $\omega_0$, but did not derive quantitative predictions. It should, however, be possible to account for the influence of these parameters by using a Landau-Zener model influenced by diagonal noise terms. Combining this with the results of Kayanuma [19, 20] would allow for more quantitative predictions.

Besides these improvements of the models presented in this thesis, there are also open questions left when it comes to the influence of noise on the Wannier-Stark system:

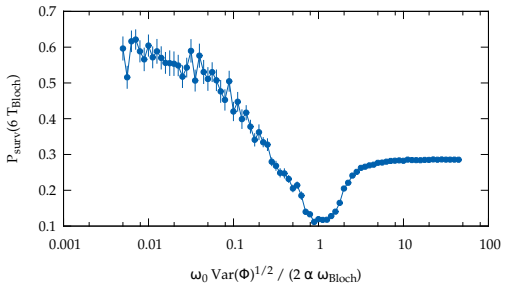


(a) Effect of amplitude noise as shown in figure 2.9

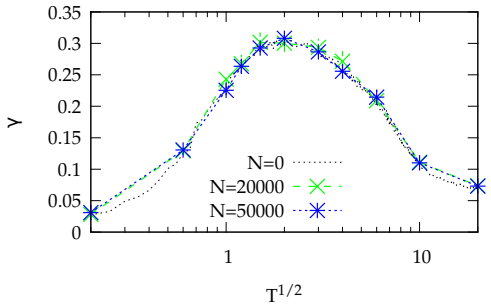


(b) Nonlinear noise-driven bichromatic Wannier-Stark system. The system parameters are identical to those used in figure 4.6, the variance of the noise process is fixed to $\langle\phi^2\rangle$.

At the end of section 4.3, we presented the results of an increased amplitude of the noise-driven lattice. While our model would predict a stronger influence of the noise lattice, the picture looks more difficult as can be seen in figure 4.7.

In section 2.4 we briefly presented a bichromatic Wannier-Stark system where the phase of both lattices is fixed, but the amplitude of one of the lattices is driven by a noise process. This system showed interesting behavior (see figure 2.9) but due to time-constraints we were not able to investigate its properties in detail.

In order to understand how stable the effects observed in chapter 4 are for real Bose-Einstein condensates for which nonlinear effects cannot be neglected, we also performed numerical simulations of the Gross–Pitaevskii equation. As can be seen in figure condensate would have on the findings in chapter 4, the tunneling rates are surprisingly robust against the presence of a moderate nonlinearity. This can be seen as a result of the relative stability of the Landau-Zener tunneling probabilities against nonlinear effects. However, we only tested this for a narrow range of parameters and further simulations should be performed in order to verify the result. It would furthermore be interesting to see the effects of the nonlinearity on the noise-free system discussed in chapter 3. We would expect to find a more discernible effect since interference effects, which seem to play an important role in this system, are strongly affected by the presence of a nonlinearity [44].

Answering these questions would also open the way to applications of the results obtained in chapter 3 for controlling the behavior of Bose-Einstein condensates experimental setups.

# Appendix

# A Generating Harmonic Noise: the Euler Maruyama Method and an Improved Algorithm

Numeric integration of stochastic differential equations is neither a straightforward nor easy task and even the best known algorithms perform very poorly when compared to their deterministic counterparts. There is a growing interest in stochastic differential equations, especially due to their use in finance leading to a wide range of literature dealing with the subject. A reader interested in this topic may have a look at [21] or [17, chapter 15] to gain a better understanding of the problems one faces when dealing with these equations. In the present work, we however only need to integrate two very specific stochastic differential equations. This allows us to implement a numeric integrator of very high quality.

Instead of directly introducing the algorithm used in this work, let us first look at the most basic method for integrating stochastic differential equations: the Euler–Maruyama method [17]. The stochastic differential equations one is usually interested in are Langevin equations of the form

$$\dot{x} = f(x,t) + u(x,t) \cdot \xi(t), \tag{A.1}$$

where $f(x,t)$ and $u(x,t)$ are known functions and $\xi(t)$ is a random white noise term with zero mean and unit variance. Here $x$ is a vector and $u(x,t)$ is a matrix whose dimension depends on the number of independent white noise terms needed for the differential equation. Integrating over time transforms (A.1) into

$$x(t+h) - x(t) = \int_t^{t+h} f(x(t'),t')dt' + \int_t^{t+h} u(x(t'),t') \cdot \xi(t')dt'. \tag{A.2}$$

Approximating the expressions inside the integrals to zeroth order through $x(t') = x(t)$ and $u(x(t'),t') = u(x(t),t)$ yields the Euler-Maruyama method:

$$\begin{aligned} x(t+h) \approx & x(t) + h\, f\,(x(t),t) + u(x(t),t) \cdot \int_t^{t+h} \xi(t')dt' && \text{(A.3)} \\ = & x(t) + h\, f\,(x(t),t) + u(x(t),t) \cdot \sqrt{h} Y_t, && \text{(A.4)} \end{aligned}$$

where $Y_t$ is a vector of Gaussian random numbers with unit Variance. The last step is possible because we know that the integral over a white noise process is akin to a random walk and therefore results in a Gaussian distribution with variance $h$. This method is known as Euler-Maruyama method and can be applied to

every stochastic differential equation [17]. It does, however, have the drawback that the approximation done in (A.3) and therefore the whole method is only accurate up to first order in $\hbar$.

The stochastic differential equations that are used for the numerical simulations in this work are the two noise-processes described in chapter 2.3:

- The exponentially correlated noise given by the equation

$$\dot{\phi} = -\Gamma\phi + \sqrt{2D\Gamma}\xi(t). \tag{A.5}$$
$$\tag{A.6}$$

  This noise has zero mean and variance $D$.

- The harmonic noise defined by the two coupled equations

$$\begin{aligned} \dot{\phi} &= \nu \\ \dot{\nu} &= -2\Gamma\nu - \omega_0^2\phi + \sqrt{4T\Gamma}\xi(t). \end{aligned} \tag{A.7}$$

  This noise process is also of zero mean and has a variance of $\frac{T}{\omega_0^2}$ (see section 2.3).

Setting $D$ and $T$ to zero reduces the stochastic differential equations to a homogeneous and deterministic form. These reduced equations are both easily solvable. The know analytic solution for the homogeneous form will allow us to find a better method for numerically integrating the stochastic equations.

We start by showing the approach for the exponential noise found in [13]. Integrating equation (A.5) results in

$$\phi(t) = e^{-t\Gamma}\phi(0) + \sqrt{2D\Gamma}\int_0^t e^{-(t-t')\Gamma}\xi(t')dt' \tag{A.8}$$
$$= e^{-t\Gamma}\phi_0 + g(t,\Gamma,D). \tag{A.9}$$

The second term $g(t,\Gamma,D)$ of this equation looks complicated but can be described by a Gaussian distribution with zero mean. This is due to the fact that any integral over a Gaussian white noise term $\xi(t)$ has to be of Gaussian nature itself[1]. The variance of this term can be easily found by comparing the variance of the left hand side of (A.9) with the known variance of the noise process. As we know that $g(t,\Gamma,D)$ is independent of $\phi(0)$, this reduces to:

$$\mathrm{Var}\left(\Phi(t)\right) = e^{-t\Gamma}\mathrm{Var}(\Phi_0) + \mathrm{Var}\left(g(t,\Gamma,D)\right) \tag{A.10}$$
$$\Leftrightarrow D = e^{-t\Gamma}D + \mathrm{Var}\left(g(t,\Gamma,D)\right) \tag{A.11}$$
$$\Rightarrow \mathrm{Var}\left(g(t,\Gamma,D)\right) = D\left(1 - e^{-t\Gamma}\right). \tag{A.12}$$

[1] An integral $\int f(t)\xi(t)dt$ can be interpreted as a sum over Gaussian variables as long as $f(t)$ is independent of $\xi(t)$ (one says that $f(t)$ should be non-anticipating). A more detailed argument can e.g. be found in [17, Chapter 4.3.5].

The random variable $g(t, \gamma, D)$ is completely described by the fact that it is Gaussian with zero mean and has a variance given by (A.12). Any process that produces Gaussian random numbers with the desired properties can be used to produce $g(t, \gamma, D)$. Given a set of Gaussian random numbers[2] $\{Y_i\}$ with unit variance and zero mean we can therefore use the method

$$\phi(t + \Delta t) = e^{-t\Gamma}\phi(t) + \sqrt{D\,(1 - e^{-t\Gamma})}Y_i. \tag{A.13}$$

to calculate $\phi(t + \Delta t)$ from $\phi(t)$.

The technique for generating the harmonic noise is analogous but slightly more complicated due to the fact that we are dealing with two coupled equations. An approach similar to the one described was first published in [34] and a more thorough description can be found in [26]. It is possible to write the two equations (A.7) as one vector equation:

$$\dot{x} = Ax + \sqrt{4T\Gamma}\begin{pmatrix} 0 \\ \xi(t) \end{pmatrix}, \tag{A.14}$$

where

$$x = \begin{pmatrix} \phi \\ v \end{pmatrix} \tag{A.15}$$

$$A = \begin{pmatrix} 0 & 1 \\ -\omega_0^2 & -2\Gamma \end{pmatrix}. \tag{A.16}$$

This eqnuation can be integrated just as the one for the exponentially correlated noise

$$x(t) = e^{At}x(0) + \sqrt{4T\Gamma}\int_0^t e^{A(t-t')}\begin{pmatrix} 0 \\ \xi(t') \end{pmatrix} dt'. \tag{A.17}$$

$$= M(t) \cdot x(0) + \alpha(t) \tag{A.18}$$

The matrix $M(t) = e^{At}$ can be calculated by diagonalizing $A$. This leads to an

[2]There are many ways to generate Gaussian random numbers numerically. The most widely used is the Box-Muller transform [2], but there are also other methods such as the Ziggurat algorithm [27].

expression of $M$ in terms of the eigenvalues $\lambda_\pm$ of $A$:

$$\lambda_\pm = -\Gamma \pm \sqrt{\Gamma^2 - \omega_0^2}, \tag{A.19}$$

$$M(t)_{1,1} = \frac{1}{\lambda_- - \lambda_+}\left(-\lambda_- e^{t\lambda_+} + \lambda_+ e^{t\lambda_-}\right), \tag{A.20}$$

$$M(t)_{2,2} = \frac{1}{\lambda_- - \lambda_+}\left(\lambda_+ e^{t\lambda_+} - \lambda_- e^{t\lambda_-}\right), \tag{A.21}$$

$$M(t)_{1,2} = \frac{1}{\lambda_- - \lambda_+}\left(e^{t\lambda_+} - e^{t\lambda_-}\right), \tag{A.22}$$

$$M(t)_{2,1} = \frac{\lambda_-\lambda_+}{\lambda_- - \lambda_+}\left(-e^{t\lambda_+} + e^{t\lambda_-}\right). \tag{A.23}$$

$$\tag{A.24}$$

The expression for the term $\alpha(t)$ of equation (A.17) can be determined in the same fashion as for $g(t)$ in (A.12). As any integral over a noise process, we know that it must be a Gaussian random variable with zero mean. All that is left to do is to find the covariance matrix. From the correlation functions given in section 2.3, we know that[3] $\langle x_1^2\rangle = T/\omega_0^2$, $\langle x_2^2\rangle = T$ and $\langle x_1 x_2\rangle = 0$.

$$\begin{aligned}\langle x_1(t)^2\rangle &= \frac{T}{\omega_0^2} = \left\langle [M\cdot x(0) + \alpha]_1^2 \right\rangle \\ &= \langle x_1(0)^2\rangle M_{1,1}^2 + \langle x_2(0)^2\rangle M_{1,2}^2 + \langle \alpha_1^2\rangle \\ &\Rightarrow \langle \alpha_1^2\rangle = \frac{T}{\omega_0^2}\left(1 - M_{1,1}^2 - \omega_0^2 M_{1,2}^2\right),\end{aligned} \tag{A.25}$$

$$\begin{aligned}\langle x_2(t)^2\rangle &= T = \left\langle [M\cdot x(0) + \alpha]_2^2 \right\rangle \\ &\Rightarrow \langle \alpha_2^2\rangle = T\left(1 - M_{2,2}^2 - \frac{M_{2,1}^2}{\omega_0^2}\right),\end{aligned} \tag{A.26}$$

$$\begin{aligned}\langle x_1(t)x_2(t)\rangle &= 0 = \langle [M\cdot x(0) + \alpha]_1 [M\cdot x(0) + \alpha]_2\rangle \\ &\Rightarrow \langle \alpha_2\alpha_1\rangle = -T\left(M_{1,2}M_{2,2} + \frac{M_{2,1}M_{1,1}}{\omega_0^2}\right),\end{aligned} \tag{A.27}$$

where for better readability, the dependence on $t$ was omitted for $M$ and $\alpha$. The desired bivariate distribution can be created by multiplying a vector $Z$ of two independent Gaussian random numbers with zero mean and unit variance with an appropriately chosen matrix $B$:

$$\alpha = B\cdot Z = \begin{pmatrix} B_{11} & 0 \\ B_{21} & B_{22}\end{pmatrix}\cdot Z. \tag{A.28}$$

[3] We can calculate the desired quantities by using the correlation functions (2.38) and setting $h = 0$.

The covariance in terms of $B$ is then

$$\begin{aligned}\langle \alpha_1^2 \rangle &= \langle (B_{11} Z_1)^2 \rangle \\ &= B_{11}^2 \langle Z_1^2 \rangle \\ &= B_{11}^2 \end{aligned} \tag{A.29}$$

$$\langle \alpha_2^2 \rangle = B_{21}^2 + B_{22}^2 \tag{A.30}$$

$$\langle \alpha_1 \alpha_2 \rangle = B_{21} B_{11}. \tag{A.31}$$

Solving these equations for $B$ results in

$$B_{11}^2 = \langle \alpha_1^2 \rangle \qquad B_{21} = \frac{\langle \alpha_1 \alpha_2 \rangle}{B_{11}} \qquad B_{22}^2 = \langle \alpha_1^2 \rangle - B_{21}, \tag{A.32}$$

which results in

$$\alpha = \begin{pmatrix} \sqrt{\langle \alpha_1^2 \rangle} & 0 \\ \frac{\langle \alpha_1 \alpha_2 \rangle}{\sqrt{\langle \alpha_1^2 \rangle}} & \sqrt{\langle \alpha_1^2 \rangle - \frac{(\langle \alpha_1 \alpha_2 \rangle)^2}{\langle \alpha_2^2 \rangle}} \end{pmatrix} \cdot Z. \tag{A.33}$$

Given a set of vectors of Gaussian random numbers $\{Z_i\}$ where each component has zero mean and variance one, the method

$$x(t + \Delta t) = M(\Delta t) \cdot x(t) + B(\Delta t) \cdot Z_i \tag{A.34}$$

can therefore be used to numerically generate a realization of the harmonic noise process.

The advantage of the methods presented here for the exponential and the harmonic noise is that they are accurate for any step size $\Delta t$. This is due to the fact that we solved the deterministic part of the equations exactly and were able to completely describe the stochastic part of the time evolution through Gaussian distributions. The Euler-Maruyama method, though simpler has an error of the order $O(\Delta t)$ and can therefore only be used for very small time steps.

It is clear that hand-crafting a method for a specific set of differential equations will usually yield a more efficient algorithm than a general purpose method can. It should, however, be noted that there are also some disadvantages to the methods presented here, especially to the one for generating harmonic noise. One disadvantage is that (A.34) requires two Gaussian random numbers per step, whereas the Euler-Maruyama method described in (A.3) only requires one. As generating random numbers is usually the most time-consuming part of the algorithm, this slows down the algorithm considerably. Especially for small $\Delta t$, the term $B_{1,1}$ in the matrix (A.33) vanishes, leading to a negligible influence of the second random number. If one is forced to generate the noise process with a small $\Delta t$, for which the accuracy of the Euler-Maruyama method is adequate, one might therefore want to choose the simpler algorithm[4].

[4] It is also possible to amend the Euler Maruyama method for the given differential equations by using the exact expression $e^{A\Delta t}$ to express the deterministic part of the propagation.

Another, more subtle disadvantage of method (A.34) is that the direct connection between the elementary noise process $\xi(t)$ and the harmonic noise is lost. As explained in chapter 2.3, integrating a stochastic differential equation actually means mapping a realization of the noise process $\xi(t)$ to a trajectory $x(t)$. This mapping is visible in the Euler-Maruyama method described by (A.3) where the term $\sqrt{h}Y_t$ represents an integral over the noise process. But in (A.34), it is not clear anymore how the vector $Z_i$ of Gaussian random numbers is connected to the elementary noise process. In the case where one is however simply interested in a robust algorithm to generate harmonic or exponentially correlated noise for any step size, the algorithms described in this chapter are far superior to the more general Euler-Maruyama method. All noise processes in this work have therefore been generated using these algorithms.

# B The Crank-Nicolson Algorithm in 2D Cylindrical Coordinates

All numerical simulations in this work were performed using the Crank-Nicolson algorithm. Even though this algorithm is well-known and can be found in most textbooks on the subject (e.g. [40]), the details of its application to the problem at hand are usually not covered and shall therefore be described here. An in-depth explanation of the details can be also found in [38, Chapter 4], from where the algorithm was adapted.

This chapter will start by briefly *deriving the Crank-Nicolson method*, followed by a short explanation about its advantages over similar methods. It will then discuss how the method can be efficiently applied to *higher dimensional problems* and especially to *problems with cylindrical symmetry*. After demonstrating how *imaginary time propagation* can be used to find the ground state of a problem, the chapter ends with a short description of how to deal with the *nonlinear Schrödinger equation*.

## The Crank-Nicolson method for one-dimensional systems

As all other finite difference methods, the Crank-Nicolson method operates by using a discrete approximation of the original differential equation. Whereas the full 1D-Schrödinger equation

$$i\frac{\partial}{\partial t}\psi(x,t) = H\psi(x,t) \tag{B.1}$$

$$H\psi(x,t) = -\frac{1}{2}\frac{\partial^2}{\partial x^2}\psi(x,t) + V(x)\psi(x,t) \tag{B.2}$$

applies to a wavefunction $\psi(x,t)$ that is defined on every point $(x,t) \in (\mathbb{R}^n \times \mathbb{R})$ in time and space, finite difference methods work by using discrete coordinates in time and space as shown in figure B.1. The wavefunction $\psi(x,t)$ is represented by its values on a set of evenly spaced points (usually called the numerical grid):

$$\begin{aligned} x_j &= x_0 + j\cdot\Delta x \qquad j \in \{0,1,\cdots,J\} \\ t_k &= t_0 + k\cdot\Delta h \qquad k \in \{0,1,\cdots,K\} \\ \psi_j(t_k) &\equiv \psi(x_j,t_k). \end{aligned} \tag{B.3}$$

Here $\Delta x$ denotes the distance between grid points in space and $\Delta t$ the distance in time. What we want our algorithm to do is to transport the wavefunction forward in time such that for a given $\psi(t_0)$ and a set of boundary conditions, we

can calculate the wavefunction at any time $t_k > t_0$. We therefore need to bring the Schrödinger equation into a form that allows us to calculate $\psi(t_k)$ from $\psi(t_{k-1})$, as displayed in figure B.1. In order to approximate the differential equation on this grid, we need to approximate the derivatives in equation (B.2) using only the values $\psi_j(t_k)$ at the grid points.

The second derivative on the left hand side of (B.2) can be easily approximated by using

$$\frac{\partial^2}{\partial x^2}\psi(x,t)|_{x_j,t_k} \approx \frac{\psi_{j-1,k} + \psi_{j+1,k} - 2\psi_{j,k}}{\Delta x^2}, \tag{B.4}$$

but the time derivative in (B.2) should be handled with more care. Simply replacing it in a similar fashion

$$\frac{\partial}{\partial t}\psi(x,t)|_{x_j,t_k} \approx \frac{\psi_{j,k+1} - \psi_{j,k}}{\Delta t} \tag{B.5}$$

would result in the so-called Forward Time Central Space (FTCS) method shown in figure B.2(a), which is not well-suited for solving the Schrödinger equation. In order to understand the reason for this, let us look at the connection to the time evolution operator $T(t, t+h)$, which for $H$ independent of $h$ is defined as

$$\psi(t+h) = T(t, t+h)\psi(t) \tag{B.6}$$

$$T(t, t+h) = \exp(-ihH). \tag{B.7}$$

Equation (B.5) is actually equivalent to using a first order expansion for $T(t, t+h)$:

$$\psi(t+h) = (1 - ihH)\,\psi(t) + O(h^2) \tag{B.8}$$

$$\Rightarrow i\frac{\psi(t+h) - \psi(t)}{h} = H\psi(t) + O(h). \tag{B.9}$$

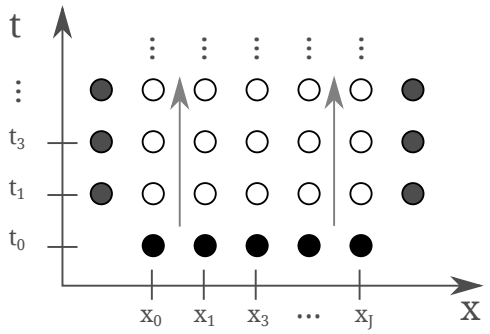


Figure B.1: Finite difference methods approximate the wavefunction using a finite number of grid points in space and time. The black circles represent the initial state at $t_0$, the gray ones the boundary conditions.

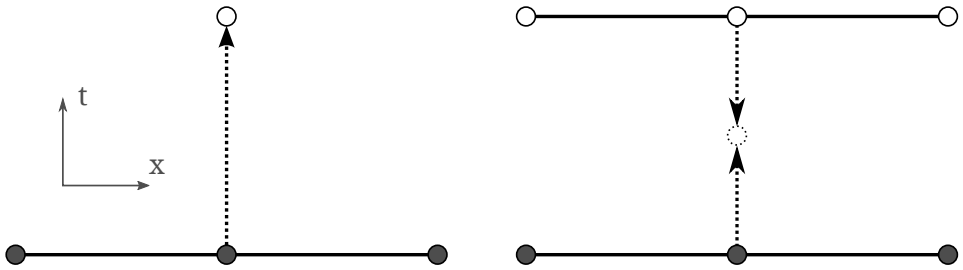


(a) The FTCS scheme (b) The Crank-Nicolson scheme

Figure B.2: Visualization of the Forward Time Center Space (FTCS) and the Crank-Nicolson scheme. The gray circles are grid points at the current time $t$, the white circles grid points at the future time $t + h$. Dotted circles represent intermediate values used during the calculation.

Given a suitable expression for $H$, this would allow us to approximate the wavefunction $\psi(t + h)$ from the wavefunction $\psi(t)$ at a previous time. However, this would not only mean introducing an error of the order $O(h)$, but also destroy any normalization. The reason for this is that the time evolution operator in (B.8) is non-unitary and therefore does not conserve normalization. A better scheme is approximating the time evolution operator in the following way (see [40, chapter 19.2]):

$$\psi(t + h) = \frac{1 - i\frac{h}{2}H}{1 + i\frac{h}{2}H}\psi(t) + O(h^3). \tag{B.10}$$

$$\Rightarrow \left(1 + i\frac{h}{2}H\right)\psi(t + h) = \left(1 - i\frac{h}{2}H\right)\psi(t) + O(h^3). \tag{B.11}$$

The accuracy of this method can be checked by Taylor-expanding the first term in (B.10) in $h$ and comparing the result with the expansion of the time evolution operator in (B.7). This approximation together with the one given in equation (B.4) defines the Crank-Nicolson method which is visualized in figure B.2b. Not only is the accuracy of this method better when compared to the method given by (B.8) but it also conserves the unitarity of the time evolution operator. It can furthermore be proven that the method is unconditionally stable for the Schrödinger equation [40, Chapter 19.2]. The method is visualized in figure B.2b.

The method described in equation (B.11) could be described as going forward half a step from $\psi(t)$, going back half a step from $\psi(t + h)$ and matching both results at $t + \frac{h}{2}$ (see figure B.2b). Unlike the explicit method to calculate $\psi(t + h)$ given in equation (B.8), this method makes it necessary to invert the operator $\left(1 + i\frac{h}{2}H\right)$. For the discrete wavefunction, this is equivalent to inverting the matrix representation of this operator. Using the wavefunction defined in (B.3) and

the approximation for its second derivative in space given in (B.4), the operator $\left(1+i\frac{h}{2}H\right)$ can be written in the following way:

$$\left[\left(1+i\frac{h}{2}H\right)\psi\right]_j = \left(1+i\frac{h}{2}V(x_j)+i\frac{1}{2h\Delta x^2}\right)\psi_j - i\frac{h}{4\Delta x^2}\psi_{j-1} - i\frac{h}{4\Delta x^2}\psi_{j+1} \tag{B.12}$$

$$= \begin{pmatrix} \ddots & & & & & \\ \alpha & 1+\beta_{i-1} & \alpha & & & \\ & \alpha & 1+\beta_i & \alpha & & \\ & & \alpha & 1+\beta_i & \alpha & \\ & & & & \ddots \end{pmatrix} \psi \tag{B.13}$$

with $\beta_j, \alpha$ defined here as

$$\begin{aligned} \beta_j &= i\frac{h}{2}V(x_j) + i\frac{h}{2\Delta x^2} \\ \alpha &= -i\frac{h}{4\Delta x^2}. \end{aligned} \tag{B.14}$$

The expression on the right hand side of equation (B.11) can similarly be written in matrix form:

$$\left(1-i\frac{h}{2}H\right)\psi = \begin{pmatrix} \ddots & & & & & \\ -\alpha & 1-\beta_{i-1} & -\alpha & & & \\ & -\alpha & 1-\beta_i & -\alpha & & \\ & & -\alpha & 1-\beta_i & -\alpha & \\ & & & & \ddots \end{pmatrix} \psi. \tag{B.15}$$

(B.16)

Equation (B.11) therefore consists of one matrix-vector multiplication and one matrix inversion. For general matrices these operations require a lot of computation (complexity $O(L^2)$ and $O(L^3)$), but the tridiagonal nature of the matrix allows both operations to be computed in $O(L)$ time using the Gauss algorithm [40].

The matrix representation of the Hamiltonian in equation (B.13) possesses an ambiguity at the boundary that we have not yet discussed. As $\psi_{-1}$ and $\psi_{L+1}$ do not exist on the grid, it is not possible to calculate the second derivative at the boundary using the approximation (B.4) used for the other grid points. We therefore chose to fix $\psi_{-1}(t) = \psi_{L+1} = 0$ in our simulations, resulting in a matrix such as the one seen in equation (B.17). The consequence is that the boundaries are reflective, which is highly artificial but necessary to be able to solve equations (B.17) and (B.18).

One step of the full Crank-Nicolson algorithm uses the wavefunction $\psi(t)$ at time $t$ to generate an approximation for the wavefunction $\psi(t+h)$ at time $t+h$. Recapitulating the last paragraphs, it is performed in the following way:

- Multiply the wavefunction $\psi(t)$ by $\left(1-i\frac{h}{2}H\right)$ to get the intermediate result $\psi(t+\frac{h}{2})$:

$$\psi(t+\frac{h}{2}) = \begin{pmatrix} 1-\beta_0 & -\alpha & & & & \\ -\alpha & 1-\beta_1 & -\alpha & & & \\ & & \ddots & & & \\ & & -\alpha & 1-\beta_{L-1} & -\alpha & \\ & & & -\alpha & 1-\beta_L \end{pmatrix} \psi(t). \tag{B.17}$$

- Solve the expression $\left(1+i\frac{h}{2}H\right)\psi(t+h) = \psi(t+\frac{h}{2})$ for $\psi(t+h)$:

$$\psi(t+\frac{h}{2}) = \begin{pmatrix} 1+\beta_0 & \alpha & & & & \\ \alpha & 1\beta_1 & \alpha & & & \\ & & \ddots & & & \\ & & \alpha & 1+\beta_{L-1} & \alpha & \\ & & & \alpha & 1+\beta_L \end{pmatrix} \psi(t+h). \tag{B.18}$$

## Operator splitting: The Crank-Nicolson method for higher dimensions

Even though many interesting quantum-mechanical phenomena can be described by one-dimensional systems, there are phenomena that can only be aptly described using higher dimensional systems. A specific example relevant for this work is the behavior of a self-interacting Bose-Einstein condensate described by the Gross–Pitaevskii equation (see chapter 2.1). Solving the Schrödinger equation in two or more dimensions requires not only a grid in more spatial dimensions, but also some adjustments to the Crank-Nicolson method. Let us first look at applying the algorithm to a two-dimensional problem. Considering the Hamiltonian of the two dimensional Schrödinger equation

$$H = -\frac{1}{2}\frac{\partial^2}{\partial x^2} - \frac{1}{2}\frac{\partial^2}{\partial y^2} + V(x,y), \tag{B.19}$$

it is clear that applying the previously explained Crank-Nicolson method would couple not only three but five grid points together. This is visualized in figure B.3a. As a consequence of this, the matrix representation of the Hamiltonian would no longer have the tridiagonal shape shown in equation (B.17) and (B.18). The performance of the algorithm does however rely on the tridiagonality of the matrix because it is exactly this property that allows us to quickly and easily invert the expression $(1+ihH/2)$.

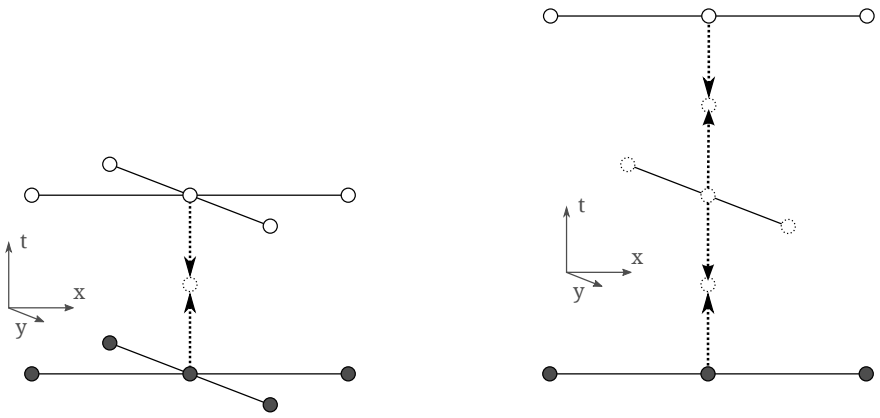


(a) Unmodified Crank-Nicolson scheme (b) Crank-Nicolson using operator splitting

Figure B.3: Using the unmodified Crank-Nicolson method shown in (a) for more than one dimension leads to a non-tridiagonal matrix. The operator splitting approach shown in (b) avoids this by splitting the time evolution operator in two tridiagonal parts.

In order to apply the Crank-Nicolson algorithm to higher dimensions, we will therefore use an approach known as *operator splitting* (also called *time splitting* or *method of fractional steps*). A general description of this approach can be found in [40]. The idea is to split the Hamiltonian into a number of summands, each of which can be written as a tridiagonal matrix. This can be accomplished by using

$$\begin{aligned} H &= H_x + H_y, \quad \text{where} \\ H_x &= \frac{1}{2}\frac{\partial^2}{\partial x^2} + V_x(x,y), \\ H_y &= \frac{1}{2}\frac{\partial^2}{\partial y^2} + V_y(x,y), \\ V(x,y) &= V_x(x,y) + V_y(x,y). \end{aligned} \tag{B.20}$$

The choice of $V_x$ and $V_y$ is arbitrary as long as the last condition holds. In some experimental setups[1], $V$ can however be split into parts that only depend on one variable each, which allows the choice $V(x,y) = V_x(x) + V_y(y)$. Hence the time evolution operator for the split Hamiltonian can be expressed as

$$\begin{aligned} T(t,t+h) &= e^{-ihH} = e^{-ihH_x - ihH_y} \\ &= \frac{1}{1+i\frac{h}{2}H_x}\left(1 - i\frac{h}{2}H_y\right)\frac{1}{1+i\frac{h}{2}H_y}\left(1 - i\frac{h}{2}H_x\right) + O(h^3). \end{aligned} \tag{B.21}$$

[1]This condition is fulfilled in many experimental setups of optical lattices. Since the containment of the Bose Einstein condensate is achieved through harmonic traps in each of the spatial directions. For an example see [35] and [47].

The ordering of the terms in equation (B.21) makes sure that even if $H_x$ and $H_y$ do not commute, the error remains of order $O(h^3)$. This means that using this split Hamiltonian introduces no additional error when compared to the one-dimensional Crank-Nicolson method. Each term of equation (B.21) can be written as either *multiplication with* or *inversion of* a tridiagonal matrix. Splitting the Hamiltonian therefore allows us to apply the Crank-Nicolson algorithm to higher dimensional problems without losing either the advantage of the tridiagonal matrices or precision. In figure B.3b, each one of these factors is represented by a dotted arrow. Each of these arrows connects an intermediate point with only three other grid points, showing the tridiagonal nature of the operations.

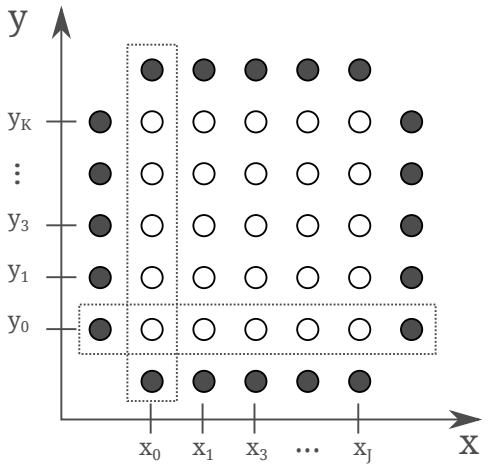


Figure B.4: Using the time-splitting method, each operator only acts on either the rows or columns of the two-dimensional grid. The grey circles represent the boundary conditions.

Let us have a more detailed look at the split operators. We define the two-dimensional numerical grid analogously to the one-dimensional one described in (B.3) as

$$\begin{aligned} x_j &= x_0 + j \cdot \Delta x & j &\in \{0, 1, \cdots, J\} \\ y_k &= y_0 + k \cdot \Delta y & k &\in \{0, 1, \cdots, K\} \\ t_m &= t_0 + m \cdot \Delta h & k &\in \{0, 1, \cdots, M\} \\ \psi_{j,k}(t_m) &\equiv \psi(x_j, y_k, t_m). \end{aligned} \tag{B.22}$$

Using this grid, the operator $(1 - ihH_x/2)$ can be written as

$$\begin{aligned} \left[\left(1 - i\frac{h}{2}H_x\right)\psi\right]_{j,k} = \left(1 - i\frac{h}{2}V(x_j, y_k) - i\frac{1}{2h\Delta x^2}\right)\psi_{j,k} \\ + i\frac{h}{4\Delta x^2}\psi_{j-1,k} + i\frac{h}{4\Delta x^2}\psi_{j+1,k}. \end{aligned} \tag{B.23}$$

This operator only couples grid points $\psi_{j,k}$ with the same index $k$. It can therefore be applied to each row of the grid independently, as seen in figure B.4. Apart from $V_{j,k} = V(x_j, y_k)$ which might depend on $k$, applying the operator to each row-vector of the grid is done using exactly the same matrix (B.17) as in the one-dimensional case. Similarly the operator $(1 + \mathrm{i}hH_x/2)^{-1}$ is applied independently to each row-vector. The operators $(1 - \mathrm{i}hH_y/2)$ and $(1 + \mathrm{i}hH_y/2)^{-1}$ on the other hand are applied to the column-vectors of the grid, but nevertheless have the same form as described in (B.17).

While retaining the tridiagonal shape of the matrices means that the method should not be slower than the one used for one-dimensional systems, this comes with a caveat. Any computation on a two-dimensional system will of course be slower in the sense that the computations needed for one time step scale with the number of grid points. As the grid now has to cover an additional dimensions, the number of grid points needed will usually be much higher than for a one-dimensional systems. For most problems one will end up with $O(N^2)$ grid points where for one dimension $N$ were sufficient. In addition, the operator splitting results in four instead of two applied operators per time step. This implies another slowdown by a factor of two.

In summary, operator splitting allows the Crank-Nicolson algorithm to be applied to two-dimensional problems without loss of accuracy and only a small loss in speed. It consists of four steps, where each step corresponds to one of the operators in equation (B.21):

- Apply the operator $\left(1 - \mathrm{i}\frac{h}{2}H_x\right)$ to each row-vector of the grid. The matrix-representation of this operator is the same as in equation (B.17), but the value of $V(x_j, y_k)$ might be different for every row of the grid;

- Apply the operator $\left(1 + \mathrm{i}\frac{h}{2}H_y\right)^{-1}$ to each column-vector of the grid. This is done by solving the same matrix-inversion problem as in equation (B.18), but with $\Delta x$ replaced by $\Delta y$ and the appropriate values for $V(x_j, y_k)$ instead;

- Applying the operator $\left(1 - \mathrm{i}\frac{h}{2}H_y\right)$ is done using the matrix given in equation (B.17) to the column-vector, but using the substitutions outlined in the previous step;

- The last step, involves solving the inverse matrix problem described in equation (B.18), but this time for the row-vectors.

Generalizing to higher dimensions is done in the same way, as long as one makes sure that the ordering of the split operators does not introduce additional errors. In a three dimensional Cartesian coordinate system, the ordering would be the

following:

$$\begin{aligned}\psi(x,y,z,t+h) = &\left(1-i\frac{h}{2}H_z\right)^{-1}\left(1-i\frac{h}{2}H_y\right)\\ &\left(1-i\frac{h}{2}H_x\right)^{-1}\left(1-i\frac{h}{2}H_x\right)\\ &\left(1-i\frac{h}{2}H_y\right)^{-1}\left(1-i\frac{h}{2}H_z\right)\psi(x,y,z,t).\end{aligned} \tag{B.24}$$

## Cylindrical coordinates for cylindrically symmetric problems

In this work, we are especially interested in applying the Crank-Nicolson method to cylindrically symmetric problems. These kind of problems lend themselves to cylindrical coordinate systems where the $x$-coordinate remains unchanged, but $y$ and $z$ are represented using $\rho$ and $\phi$:

$$\begin{aligned}x &= x\\ y &= \rho\sin(\phi)\\ z &= \rho\cos(\phi)\end{aligned} \tag{B.25}$$

This coordinate system poses new problems:

- The Schrödinger equation does change its form due to the non-Cartesian nature of the coordinate system;
- At the coordinate $\rho = 0$, the coordinate system has a singularity that has to be dealt with.

Nevertheless, this coordinate system provides huge advantages for cylindrically symmetric problems. Assuming that the wavefunction $\psi(x,\rho,\phi)$ is independent of $\phi$ allows one to reduce the three-dimensional problem to two dimensions. This reduces the time and memory needed for the calculations by a large factor because the wavefunction only needs to be defined on a two-dimensional grid:

$$\begin{aligned}x_j &= x_0 + j\cdot\Delta x \qquad j\in\{0,1,\cdots,J\}\\ \rho_k &= k\cdot\Delta\rho \qquad\quad k\in\{0,1,\cdots,R\}\\ \psi_{j,k} &\equiv \psi(x_j,\rho_k).\end{aligned} \tag{B.26}$$

The assumption of a cylindrically symmetric wavefunction also allows us to identify $\psi(x,-\rho)$ with $\psi(x,+\rho)$. This reduces the needed storage space and the size of the matrix representations of the Hamiltonian by a factor of one half.

The Hamiltonian in cylindrical coordinates reads

$$H = -\frac{1}{2}\left(\frac{\partial^2}{\partial x^2}+\frac{\partial^2}{\partial\rho^2}+\frac{1}{\rho}\frac{\partial}{\partial\rho}+\frac{1}{\rho^2}\frac{\partial^2}{\partial\phi^2}\right)+V(x,\rho,\phi). \tag{B.27}$$

In the case of a cylindrically symmetric wavefunction we can assume the derivative with respect to $\phi$ to vanish. The remaining Hamiltonian can then be split into

$$H_\rho = -\frac{1}{2}\left(\frac{\partial^2}{\partial\rho^2} + \frac{\partial}{\rho\partial\rho}\right) + V_\rho(x,\rho) \quad \text{and} \tag{B.28}$$

$$H_x = -\frac{1}{2}\frac{\partial^2}{\partial x^2} + V_x(x,\rho). \tag{B.29}$$

The first derivative with respect to $\rho$ in equation (B.28) can be approximated through

$$\frac{\partial}{\partial\rho}\psi(x,\rho)|_{x,\rho} = \frac{\psi(x,\rho+\Delta\rho) - \psi(x,\rho-\Delta\rho)}{2\Delta\rho}. \tag{B.30}$$

This additional term in the radial part of the Hamiltonian does not destroy the tridiagonal form, as it only depends on the two neighboring grid points in the $\rho$-direction.

At $\rho = 0$, evaluating (B.28) becomes problematic as the term $\frac{\partial}{\rho\partial\rho}$ is not well-defined. Luckily the restriction to cylindrically symmetric wavefunctions can help us circumvent this problem. Due to the symmetry of the wavefunction we know that $\phi(x,\rho) = \phi(x,-\rho)$. Therefore the first derivative with respect to $\rho$ at $\rho = 0$ has to vanish. Using L'Hôsptial's rule we can thus rewrite the expression as

$$\begin{aligned}\lim_{\rho\to 0}\frac{\frac{\partial}{\partial\rho}}{\rho} &= \lim_{\rho\to 0}\frac{\frac{\partial}{\partial\rho}\frac{\partial}{\partial\rho}}{\frac{\partial}{\partial\rho}\rho} \\ &= \lim_{\rho\to 0}\frac{\partial^2}{\partial\rho^2} \quad ,\end{aligned} \tag{B.31}$$

which allows us to write the Hamiltonian in a well-defined way at $\rho = 0$.

Using equation (B.31) and (B.30) and the fact that $\phi(x,-\rho) = \phi(x,\rho)$, we can write the radial part of the Hamiltonian in the following form:

$$\begin{aligned} H\psi_{j,0} &= -\frac{2\psi_{j,1} - 2\psi_{j,0}}{\Delta\rho^2} + V_{j,0} && k = 0 \\ H\psi_{j,k} &= -\frac{1}{2}\frac{\psi_{j,k+1} + \psi_{j,k-1} - 2\psi_{j,k}}{\Delta\rho^2} \\ &\quad - \frac{1}{2k\Delta\rho}\frac{\psi_{j,k+1} - \psi_{j,k-1}}{2\Delta\rho} + V_{j,0} && k \neq 0 \end{aligned} \tag{B.32}$$

The matrix form of $(1 \pm i\hbar H_\rho/2)$ thus is

$$1 \pm i\frac{h}{2}H_\rho = \begin{pmatrix} 1\pm\gamma & \pm\eta & & & \\ \pm\alpha_1 & 1\pm\beta_1 & \pm\delta_1 & & \\ & & \ddots & & \\ & & \pm\alpha_{R-1} & 1\pm\beta_{R-1} & \pm\delta_{R-1} \\ & & & \pm\alpha_R & 1\pm\beta_R \end{pmatrix}, \tag{B.33}$$

where

$$\begin{aligned}
\gamma &= \frac{ih}{\Delta\rho^2} + \frac{ih}{2}V_\rho(0),\\
\beta_k &= \frac{ih}{2\Delta\rho^2} + \frac{ih}{2}V_\rho(k\Delta\rho),\\
\eta &= -\frac{ih}{\Delta\rho^2},\\
\alpha_k &= -\frac{ih}{4\Delta\rho^2} + \frac{1}{8k\Delta\rho^2},\\
\delta_k &= -\frac{ih}{4\Delta\rho^2} - \frac{1}{8k\Delta\rho^2}.
\end{aligned} \tag{B.34}$$

We can see that for $\rho \to \infty$, the secondary diagonal terms $\alpha_i$ and $\delta_i$ converge against the term $\alpha$ for Cartesian coordinate systems found in (B.14). This is in line with the expectation that at large $\rho$ the cylindrical coordinates are locally similar to Cartesian coordinates.

Apart from the different matrix $(1 \pm ihH_\rho/2)$, applying the Crank-Nicolson method in cylindrical coordinates is done in the same way as described on page 78 for Cartesian coordinates. One simply has to replace the matrix $(1 \pm ihH_y/2)$ by $(1 \pm ihH_\rho/2)$.

## Finding the ground state of a system with imaginary time propagation

In experimental setups like the one introduced in section 2.4, the Bose-Einstein condensate is usually assumed to be in the ground state of the system at the start of the experiment. Yet, for most potentials and nonlinearities no analytic expression for the ground state is known, making it necessary to compute it numerically. It is possible to employ the Crank-Nicolson method for this by using a technique known as imaginary time propagation. The way this technique works can be easily understood by comparing it with the Schrödinger equation. Assuming a complete set of energy eigenstates $\{E_i, \Phi_i\}$, consider the effect of the following differential equations on an arbitrary state $\psi = \sum_i \alpha_i \Phi_i$:

$$\begin{aligned}
i\frac{\partial}{\partial t}\psi &= H\psi\\
\Rightarrow \dot{\alpha}(t) &= -iE_i\alpha(0)
\end{aligned} \tag{B.35}$$

and the similar equation

$$\begin{aligned}
-\frac{\partial}{\partial t}\psi &= H\psi\\
\Rightarrow \dot{\alpha}(t) &= -E_i\alpha(0)
\end{aligned} \tag{B.36}$$

Equation (B.35) is just the Schrödinger equation and the coefficients $\alpha_i(t)$ of its solution rotate around the origin of the complex plane with a frequency proportional to the energy $E_i$ of their respective energy eigenstate. Equation (B.36) on the other hand results from replacing the time $t$ in the Schrödinger equation by the term $-it$. The coefficients $\alpha_i$ of its solution behave in a much simpler way: they simply grow or shrink exponentially, depending on the energy eigenvalue $E_i$ of $\Phi_i$.

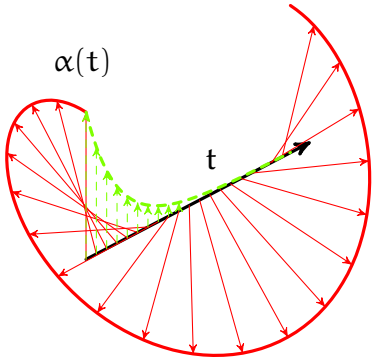


Figure B.5: Illustration of the imaginary time algorithm: While the Schrödinger equation rotates the state around the imaginary axis (red), the imaginary time equation leads to an exponential decay (green).

It is clear that the coefficient $\alpha_0$ of the lowest energy eigenstate $\Phi_0$ will grow exponentially in time, when compared to the coefficients of all other eigenstates. This means taking any state $\psi$ with $\alpha_0 \neq 0$, subjecting it to the time evolution under equation (B.36) for a time $t$ and finally renormalizing it such that $\sum_i |\alpha_i|^2 = 1$ will result in a state $\psi'$ very close to the ground state $\Phi_0$. The time $t$ needed for calculating the ground state with a given accuracy is inversely proportional to the energy difference $E_1 - E_0$ between the ground state and the first excited state:

$$\frac{\alpha_1(t)}{\alpha_0(t)} = \frac{\alpha_1(0)}{\alpha_0(0)} e^{-(E_1 - E_0)t}. \tag{B.37}$$

This method allows us to easily find the ground state for general potentials in arbitrary spatial dimensions. In order to assure that the result has converged on the ground state,it is possible to wait until the changes of the wavefunction over time fall below a certain threshold.

## A simple predictor corrector method for the nonlinear Schrödinger equation

In this work, the Crank-Nicolson algorithm in cylindrical coordinates will be mainly used to integrate the Gross–Pitaevskii equation, which is a nonlinear ver-

sion of the Schrödinger equation:

$$i\frac{\partial}{\partial t}\psi(x,t) = -\frac{1}{2}\frac{\partial^2}{\partial x^2}\psi(x,t) + \left(V(x,t) + U\,|\psi(x,t)|^2\right)\psi(x,\rho,t). \tag{B.38}$$

The reason we did not account for the nonlinear term $U\,|\psi(x,t)|^2$ yet is that it can be absorbed into the potential $V(x,t)$ without needing to change the algorithm. We can therefore use the algorithm developed in this chapter by simple replacing $V(x,\rho,t)$ by a modified potential $\tilde{V}$:

$$V'(x,\rho,t) = V(x,\rho,t) + U|\psi(x,\rho,t)|^2. \tag{B.39}$$

The wavefunction and therefore the nonlinear term does however not remain constant during a step of the Crank-Nicolson algorithm. Incorporating this into the method is not straightforward.

The easiest way would be to evaluate the term $|\psi(x,\rho)|^2$ at the beginning of each step and let the potential $V'$ remain constant until the beginning of the next step. This would be equivalent to the Euler method for ordinary differential equations, which only uses information from the beginning of each time step. The estimate that the nonlinear term $|\psi(x,\rho,t)|^2$ remains constant will, however, have acquired some error at the time $t+\Delta t$.

In order to gain accuracy and stability, we will therefore use a predictor-corrector scheme similar to the two-step Runge Kutta method:

- Set $V'(x,\rho,t) = V(x,\rho,t) + U|\psi(x,\rho,t)|^2$ and use the Crank-Nicolson method to compute a predicted value $\psi'(x,\rho,t+\Delta t)$.
- Use an updated term $\tilde{V}$ that averages between the original and the predicted value of the nonlinear term:

  $$\tilde{V} = V(x,\rho,t) + \frac{U}{2}\left(|\psi(x,\rho,t)|^2 + \psi'(x,\rho,t+\Delta t)|^2\right). \tag{B.40}$$

  Repeat the previous step with this term $\tilde{V}$ instead of $V'$ to calculate the final value $\psi(x,\rho,t+\Delta t)$.

Just as the two-step Runge-Kutta method performs by an order of $O(\Delta t)$ better than the Euler method, we would estimate that this predictor-corrector method improves the accuracy by a similar magnitude. The disadvantage of this method is that every time step has to be performed twice, halving the overall speed of the algorithm. Additionally the amount of memory needed is increased by the need to keep two copies of the wavefunction in memory.

It is possible to generalize this method to more than one predictor step without problems. This results however in a further slowdown as more intermediate copies of the wavefunction have to be computed and held in memory. For most purposes using one intermediate step should be enough, but it is of course necessary to check that the method has converged. This can be done by comparing the results of the calculations when using different time steps $\Delta t$.

There are many other methods that allow applying the Crank-Nicolson method to the nonlinear Schrödinger equation. Another method very similar to the one explained here, but without the loss in speed can be found in [6].

# C Bibliography


[1] N. Ashcroft and N. Mermin. *Solid state physics*. Holt-Saunders International Editions: Science : Physics. Holt, Rinehart and Winston, 1976.

[2] G. E. P. Box and M. E. Muller. A note on the generation of random normal deviates. *The Annals of Mathematical Statistics*, 29(2):pp. 610–611, 1958.

[3] C. C. Bradley, C. A. Sackett, J. J. Tollett, and R. G. Hulet. Evidence of Bose-Einstein condensation in an atomic gas with attractive interactions. *Physical Review Letters*, 75:1687–1690, August 1995.

[4] S. Brundobler and V. Elser. S-matrix for generalized Landau-Zener problem. *Journal of Physics A: Mathematical and General*, 26(5):1211, 1993.

[5] S. Chandrasekhar. Stochastic problems in physics and astronomy. *Rev. Mod. Phys.*, 15:1–89, Jan 1943.

[6] Q. Chang, E. Jia, and W. Sun. Difference schemes for solving the generalized nonlinear Schrödinger equation. *Journal of Computational Physics*, 148(2):397 – 415, 1999.

[7] K. B. Davis, M. O. Mewes, M. R. Andrews, N. J. van Druten, D. S. Durfee, D. M. Kurn, and W. Ketterle. Bose-Einstein condensation in a gas of sodium atoms. *Phys. Rev. Lett.*, 75:3969–3973, Nov 1995.

[8] A. Einstein. Über die von der molekularkinetischen theorie der Wärme geforderte Bewegung von in ruhenden Flüssigkeiten suspendierten Teilchen. *Annalen der Physik*, 322:549–560, 1905.

[9] A. Einstein. Quantentheorie des einatomigen idealen Gases. *Sitzungsberichte der Preußischen Akademie der Wissenschaften*, Physikalisch-mathematische Klasse:261–267, 1924.

[10] G. Ferrari, N. Poli, F. Sorrentino, and G. M. Tino. Long-lived Bloch oscillations with bosonic Sr atoms and application to gravity measurement at the micrometer scale. *Phys. Rev. Lett.*, 97:060402, Aug 2006.

[11] M. C. Fischer and M. G. Raizen. Experiments on quantum transport of ultracold atoms in optical potentials. In A. R. J.G. Muga and A. del Campo, editors, *Time in Quantum Mechanics - Vol. 2*. Springer Berlin Heidelberg, 2010.

[12] T. Fließbach. *Statistische Physik: Lehrbuch Zur Theoretischen Physik IV*. Fließbach, Torsten: Lehrbuch zur theoretischen Physik. Spektrum Akademischer Verlag, 2010.

[13] R. F. Fox, I. R. Gatland, R. Roy, and G. Vemuri. Fast, accurate algorithm for numerical simulation of exponentially correlated colored noise. *Phys. Rev. A*, 38:5938–5940, Dec 1988.

[14] M. Frigo and S. G. Johnson. The design and implementation of FFTW3. *Proceedings of the IEEE*, 93(2):216–231, 2005. Special issue on "Program Generation, Optimization, and Platform Adaptation".

[15] M. Galassi, J. Davies, J. Theiler, B. Gough, G. Jungman, M. Booth, and F. Rossi. *Gnu Scientific Library: Reference Manual*. Network Theory Ltd., February 2003.

[16] L. Gammaitoni, P. Hänggi, P. Jung, and F. Marchesoni. Stochastic resonance: A remarkable idea that changed our perception of noise. *The European Physical Journal B - Condensed Matter and Complex Systems*, 69:1–3, 2009. 10.1140/epjb/e2009-00163-x.

[17] C. W. Gardiner. *Stochastic methods*. Number [13] in Springer series in synergetics ; [13] ; Springer complexity ; Springer series in synergetics. Springer, Berlin ; Heidelberg, 4. ed. edition, 2009. Includes bibliographical references and index. - Previous ed.: 2004.

[18] M. Gustavsson, E. Haller, M. J. Mark, J. G. Danzl, G. Rojas-Kopeinig, and H.-C. Nägerl. Control of interaction-induced dephasing of Bloch oscillations. *Phys. Rev. Lett.*, 100:080404, Feb 2008.

[19] Y. Kayanuma. Nonadiabatic transitions in level crossing with energy fluctuation. I. analytical investigations. *Journal of the Physical Society of Japan*, 53(1):108–117, 1984.

[20] Y. Kayanuma. Nonadiabatic transitions in level crossing with energy fluctuation. II. numerical investigations. *Journal of the Physical Society of Japan*, 53(1):118–122, 1984.

[21] P. E. Kloeden and E. Platen. *Numerical solution of stochastic differential equations*. Number 23 in Applications of mathematics ; 23 ; Mathematik für das Lehramt ; Applications of mathematics. Springer, Berlin ; Heidelberg [u.a.], corr. 3. print. edition, 1999.

[22] L. D. Landau. Zur Theorie der Energieubertragung. II. *Phys Z*, 2(2):46–51, 1932.

[23] K. Leo, P. H. Bolivar, F. Brüggemann, R. Schwedler, and K. Köhler. Observation of Bloch oscillations in a semiconductor superlattice. *Solid State Communications*, 84(10):943 – 946, 1992.

[24] D. Luchinsky, R. Maier, R. Mannella, P. McClintock, and D. Stein. Observation of saddle-point avoidance in noise-induced escape. *Physical Review Letters*, 82(9):1806–1809, 1999.

[25] N. Lörch, F. V. Pepe, H. Lignier, D. Ciampini, R. Mannella, O. Morsch, E. Arimondo, P. Facchi, G. Florio, S. Pascazio, and S. Wimberger. Wave function renormalization effects in resonantly enhanced tunneling, 2012, arXiv:1201.6286.

[26] R. Mannella. La teoria della risposta lineare in sistemi stocastici caratterizzati da basso attrito, 1985.

[27] G. Marsaglia and W. W. Tsang. The Ziggurat method for generating random variables. *Journal of Statistical Software*, 5(8):1–7, 10 2000.

[28] Q. Niu and M. G. Raizen. How Landau-Zener tunneling takes time. *Phys. Rev. Lett.*, 80:3491–3494, Apr 1998.

[29] C. Pethick and H. Smith. *Bose-Einstein Condensation in Dilute Gases*. Cambridge University Press, 2002.

[30] V. L. Pokrovsky and S. Scheidl. Correlations in noisy Landau-Zener transitions. *Phys. Rev. B*, 70:014416, Jul 2004.

[31] V. L. Pokrovsky and D. Sun. Fast quantum noise in the Landau-Zener transition. *Phys. Rev. B*, 76:024310, Jul 2007.

[32] M. Rosini and L. Reggiani. Noise and diffusion in superlattices within the Wannier-Stark approach. In T. González, J. Mateos, & D. Pardo, editor, *Noise and Fluctuations - ICNF 2005*, volume 780 of *American Institute of Physics Conference Series*, pages 769–772, August 2005.

[33] Satyendra Bose. Plancks Gesetz und Lichtquantenhypothese. *Zeitschrift für Physik*, 26:178–181, December 1924.

[34] L. Schimansky-Geier, J. J. Hesse, and C. Zülicke. Harmonic noise driven bistable dynamics. *Berichte der Bunsengesellschaft für physikalische Chemie*, 95(3):349–352, 1991.

[35] C. Sias, A. Zenesini, H. Lignier, S. Wimberger, D. Ciampini, O. Morsch, and E. Arimondo. Resonantly enhanced tunneling of Bose-Einstein condensates in periodic potentials. *Phys. Rev. Lett.*, 98:120403, Mar 2007.

[36] N. A. Sinitsyn. Counterintuitive transitions in the multistate Landau–Zener problem with linear level crossings. *Journal of Physics A: Mathematical and General*, 37(44):10691, 2004.

[37] S. M. Soskin, V. I. Sheka, T. L. Linnik, and R. Mannella. Short time scales in the Kramers problem: A stepwise growth of the escape flux. *Phys. Rev. Lett.*, 86:1665–1669, Feb 2001.

[38] G. Tayebirad. Engineering the Landau-Zener tunneling of ultracold atoms in tilted potential, 2011. Ph.D. Thesis,University of Heidelberg.

[39] G. Tayebirad, R. Mannella, and S. Wimberger. Engineering interband transport by time-dependent disorder. *Phys. Rev. A*, 84:031605, Sep 2011.

[40] W. T. Vetterling, S. A. Teukolsky, B. P. Flannery, and W. H. Press. *Numerical Recipes Example Book C++*. Cambridge University Press, New York, NY, USA, 2nd edition, 2002.

[41] N. V. Vitanov. Transition times in the Landau-Zener model. *Phys. Rev. A*, 59:988–994, Feb 1999.

[42] M. C. Wang and G. E. Uhlenbeck. On the theory of the brownian motion II. *Rev. Mod. Phys.*, 17:323–342, Apr 1945.

[43] D. S. Wiersma, P. Bartolini, A. Lagendijk, and R. Righini. Localization of light in a disordered medium. *Nature*, 390:671–673, December 1997.

[44] S. Wimberger, P. Schlagheck, and R. Mannella. Tunnelling rates for the nonlinear Wannier–Stark problem. *Journal of Physics B: Atomic, Molecular and Optical Physics*, 39(3):729, 2006.

[45] C. Wittig. The Landau-Zener formula. *The Journal of Physical Chemistry B*, 109(17):8428–8430, 2005. PMID: 16851989.

[46] C. Zener. Non-Adiabatic Crossing of Energy Levels. *Royal Society of London Proceedings Series A*, 137:696–702, September 1932.

[47] A. Zenesini, H. Lignier, G. Tayebirad, J. Radogostowicz, D. Ciampini, R. Mannella, S. Wimberger, O. Morsch, and E. Arimondo. Time-resolved measurement of Landau-Zener tunneling in periodic potentials. *Phys. Rev. Lett.*, 103:090403, Aug 2009.

Erklärung:

Ich versichere, dass ich diese Arbeit selbstständig verfasst habe und keine anderen als die angegebenen Quellen und Hilfsmittel benutzt habe.

Heidelberg, den (Datum) .....